

**SIMULATING COLLISIONAL DARK  
MATTER USING A LATTICE  
BOLTZMANN METHOD**

**Javier Alejandro  
Acevedo Barroso**

**Advisor:  
Dr. Jaime E. Forero-Romero**

A monograph presented for the degree of Physicist.



Departamento de Física  
Facultad de Ciencias  
Universidad de los Andes  
Bogotá, Colombia

November, 2018

## *Dedicado a*

*Mi mamá, pues sin su paciencia y consejo nunca lo habría logrado.*

*Mi papá, quién me enseñó el valor del arte, la ciencia y la amistad.*

*Susana, por la inolvidable vida que hemos compartido.*

# Simulating Collisional Dark Matter Using a Lattice Boltzmann Method

Javier Alejandro Acevedo Barroso

November, 2018

## Abstract

Usually, dark matter is simulated with N-body schemes that sample the phase space in order to solve the Poisson-Vlasov equation. These kind of simulations have been essential for the development of modern cosmology and the characterization of dark matter halos. With the development of particle physics, we ultimately expect dark matter to be a particle outside of the standard model of physics. Recent measurements on the aftermath of galaxy cluster collisions allow us to constrain the value of the thermally averaged cross section  $\langle\sigma v\rangle$ , thus motivating the development of dark matter *collisional* simulations.

On the other hand, Lattice-Boltzmann simulations have been widely used to recreate increasingly complex fluids and boundary conditions, nonetheless, the usual Lattice-Boltzmann scheme does not simulate the entirety of the velocity space, but simply a small number of advective velocities.

Inspired by the work of Philip Mocz, Sauro Succi [1], and Sebastian Franco [2], in which a Lattice-Boltzmann scheme is used to simulate the phase space of a *collisionless* one dimensional dark matter fluid. We implement a Lattice-Boltzmann simulations of the phase space of a *collisional* one, two, and three dimensional dark matter fluid. For the collisional step, we use the BGK approximation modeled by a relaxation time  $\tau$  chosen accordingly to recent measurements of the  $\langle\sigma v\rangle$ .

# Simulando Materia Oscura Colisional Utilizando un Método de Lattice Boltzmann

Javier Alejandro Acevedo Barroso

Noviembre, 2018

## Resumen

Usualmente la materia oscura se simula con métodos de N cuerpos, en los que se muestrea el espacio de fase con el fin de resolver la ecuación de Poisson-Vlasov.

Este tipo de simulaciones ha sido esencial tanto para el desarrollo de la cosmología moderna, como para la caracterización de los halos de materia oscura. Con el desarrollo de la física de partículas, esperamos que en últimas la materia oscura sea una partícula fuera del modelo estandar. Mediciones recientes del resultado de colisiones entre cúmulos galácticos, permiten dar límites para los valores del promedio térmico de la sección transversal  $\langle\sigma v\rangle$ , motivando el desarrollo de simulaciones colisionales de materia oscura.

Por otro lado, las simulaciones de Lattice-Boltzmann han sido ampliamente utilizadas para recrear fluidos cada vez más complejos. Sin embargo, la implementación usual no simula el espacio de velocidades en sí, sino un pequeño número de velocidades adventivas.

Inspirados en el trabajo realizado por Philip Mocz, Sauro Succi [1], y Sebastián Franco [2], en donde se simula el espacio de fase de un fluido *no colisional* de materia oscura en una dimensión. Implementamos un método de Lattice-Boltzmann para simular un fluido *colisional* de materia oscura en una, dos y tres dimensiones. Para el paso colisional usamos la aproximación BGK modelada por un tiempo de relajación  $\tau$ , seleccionado de acuerdo a mediciones recientes de  $\langle\sigma v\rangle$ .

# Agradecimientos

Agradezco profundamente a Jaime Forero, por su guía, paciencia y visión en el desarrollo de esta monografía. A Sebastián Franco, por sentar muy bien las bases de este proyecto. Y a todos los se convirtieron en mis amigos en estos años de estudio.

# Contents

<b>1</b>	<b>Introduction</b>	<b>1</b>
1.1	Dark Matter . . . . .	1
1.1.1	The missing mass problem in Galaxy Clusters . . . . .	2
1.1.2	Galaxy Rotation Curves . . . . .	3
1.1.3	The Bullet Cluster . . . . .	5
1.2	Particle Dark Matter . . . . .	7
1.3	The Boltzmann Equation . . . . .	9
1.4	Lattice Boltzmann Method . . . . .	10
1.5	BGK Approximation . . . . .	11
<b>2</b>	<b>The Lattice Boltzmann Algorithm</b>	<b>13</b>
2.1	General Description . . . . .	13
2.2	The Collisional Step . . . . .	17
2.2.1	Parameters of the simulation . . . . .	21
2.3	Initial Conditions . . . . .	23
<b>3</b>	<b>Numerical Tests</b>	<b>26</b>
3.1	Two dimensional phase space . . . . .	26

3.2	Four dimensional phase space	33
3.3	Six dimensional phase space	38
<b>4</b>	<b>Results</b>	<b>42</b>
4.1	The two dimensional phase space	42
4.1.1	Collisional Gaussian distribution	42
4.1.2	The Bullet Cluster	45
4.2	The four dimensional phase space	52
<b>5</b>	<b>Conclusions</b>	<b>55</b>
<b>6</b>	<b>Bibliography</b>	<b>58</b>

# Chapter 1

## Introduction

In order to follow the ideas and developments of the upcoming chapters, it is essential to understand some concepts and computational techniques. In this chapter, we discuss all the necessary knowledge for the proper understanding of this work.

### 1.1 Dark Matter

Modern cosmology describes the universe as being dominated by two fundamental components: dark energy and matter<sup>1</sup>. Dark energy is usually associated with a cosmological constant.

We know of the existence of dark matter entirely from astronomical evidence. In this section we review some of these observations.

---

<sup>1</sup>In relativity, mass and energy are equivalent.

### 1.1.1 The missing mass problem in Galaxy Clusters

The traditional history of dark matter begins in the 1930s with the swiss astronomer Fritz Zwicky[3] [4], who measured an unusually high velocity dispersion between the galaxies of the Coma Cluster. To tackle the problem, Zwicky assumed that the Coma Cluster “had already reached a mechanically stationary state” [5] and such, the virial theorem could be applied. By counting galaxies, along with assuming that matter is distributed uniformly in the cluster and using Hubble’s estimate of the mean mass of a galaxy, Zwicky was able to estimate the potential energy of the Cluster. Using his estimate of the visible mass and the virial theorem, Zwicky concluded that the velocity dispersion had to be close to  $\sqrt{v^2} = 80$  km/s. Nonetheless, the real measurement of the velocity dispersion was  $\sqrt{v^2} = 1000$  km/s, implying a virial mass about 400 times larger than the visible mass<sup>2</sup>. Zwicky called the discrepancy between the luminous matter (in the form of visible galaxies which could simply be counted) and the virial matter (obtained from the virial theorem and the high velocity dispersion of the cluster) “Dark Matter”.

By the late 1950s similar calculations for different clusters had been published. Many of those calculations had very large values for the mass-to-light ratio[6], which were consistent with the mass-to-light ratio calculated from the Coma Cluster. The problem of the missing mass seemed to appear in almost every large scale structure in the universe, and by the early 1970s astrophysicist had already disregarded hot gas[7] and free hydrogen[8] as explanations for the missing mass in Clusters. Nonetheless, it was still possible that the missing mass problem could be in fact solved by a more refined model of the cluster kinematics, because by then, the missing mass problem

---

<sup>2</sup>This ratio is known as the mass-to-light ratio.

had only been observed on Galaxy Clusters and large scale structures.

### 1.1.2 Galaxy Rotation Curves

A galaxy rotation curve plots the orbital velocity of stars in a galaxy versus their distance to the galaxy centre. These curves became very informative thanks to the work of the Indian astrophysics Subrahmanyan Chandrasekhar, who proved that the mutual interactions between stars were negligible, so a galaxy could be modeled accurately as a non-interacting system of stars [9]. Such modeling allows to obtain mass profiles from galaxy rotation curves. Now, due to photometric measurements, astrophysicist believed that most of galaxy's mass was overwhelmingly concentrated in the galaxy centre, therefore, it was reasonable to model the galaxy similarly to the solar system.

Consider a star in the galaxy disk with mass  $m$  at a distance  $r$  from the galaxy centre. Given that we can disregard the interaction between starts, the sum of forces acting on the object is simply the gravitational attraction towards the centre of the galaxy:

$$m \frac{v^2}{r} = G \frac{mM}{r^2}, \quad (1.1)$$

with  $M$  being the mass enclosed by the star orbit and  $v$  being the orbital velocity of the star. Finally, the galaxy rotation curve for such galaxy will be given by

$$v(r) = \sqrt{\frac{GM}{r}}. \quad (1.2)$$

Which means that for objects outside of the galaxy disk (but still under the influence

## 1.1. DARK MATTER

---

of the galaxy gravitational pull) the enclosed mass will be constant regardless of the radius, and thus, the orbital velocity will be proportional to  $r^{-1/2}$ . With the advent of radio astronomy and the invention of the Image Tube Spectrograph, astronomers were able to measure orbital velocities way beyond the apparent end of the luminous galaxy disks, only to find that the orbital velocity did not decay proportionally to  $r^{-1/2}$  but it stayed more or less constant[10] [11] [12]. This behavior can be seen easily in the figure 1.1:

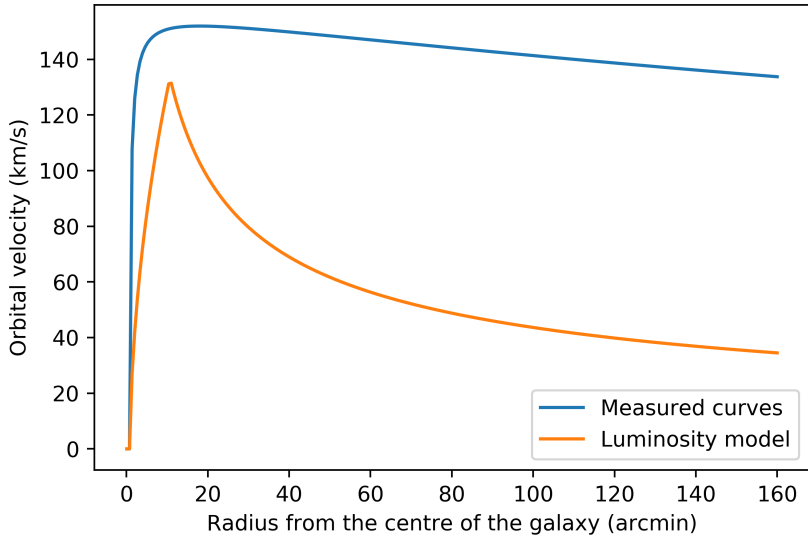


Figure 1.1: A comparison between the model from photometrical measurements and the curves measured. These curves are simulated and do not correspond to any particular galaxy.

This unexpected velocity profile implied a mass-to-light ratio that increased with distance and also the existence of mass beyond the visible galactic disk[13]. The overwhelming amount of high quality galaxy rotation curves measured during the 1970s, led to the acceptance of the dark matter hypothesis in the astrophysical com-

munity.

Throughout the use of numerical simulations and the measurement of more galaxy rotation curves during the 1980s and the 1990s, it was concluded that the dark matter density in galaxies was well modeled by the Navarro-Frenk-White (NFW) profile:[14][15]

$$\rho(r) = \frac{\rho_0}{r/r_s(1+r/r_s)^2}. \quad (1.3)$$

### 1.1.3 The Bullet Cluster

Galaxy clusters have three main constituents: dark matter, intracluster gas (which is mostly ionised hydrogen and helium), and the galaxy themselves.[16]

We can observe the intracluster baryonic matter in the X-ray band thanks to Bremsstrahlung radiation, therefore, by doing photometry in X-ray it is possible to map the baryonic gas distribution in a cluster. In the case of dark matter, we infer its existence in clusters thanks to the work of Fritz Zwicky and the posterior work in the missing mass problem in galaxy clusters. Our current estimates place most of the cluster mass in the dark matter component. By analyzing the gravitational lensing effect (in particular the *weak* gravitational lensing effect) it is possible to map the mass distribution of a galaxy cluster. Lastly, we can observe the galaxies in the visual and the infrared band. They are the only component of a galaxy cluster that can be observed in the visual band. About 90 percent of the mass of a cluster is dark matter (this is not a surprise since Fritz Zwicky measured mass-to-light ratios of 50 during the 1930s). Of the remaining baryonic matter, the ionized gas mass can represent up to 90% of the baryonic mass, making galaxies responsible for about 1% of the total

## 1.1. DARK MATTER

---

cluster mass.

The object Bullet Cluster (also known as 1E 0657-558) is the aftermath of the collision of two galaxy cluster. Before the collision, each cluster had its own set galaxies, baryonic gas and dark matter, and the centroid of each constituent coincided with the center of mass of the whole cluster. During the collision, each constituent reacts differently to the situation:

- Galaxies, given that they occupy a minuscule fraction of the total volume of the cluster, are essentially collisionless. Two galaxy clusters can collide without any galaxy (or very little galaxies) colliding per se.
- Dark matter is also modeled as collisionless, therefore, during the collision of two galaxy clusters, the dark matter components simply pass through, similarly to how Neutrinos constantly cross the Earth without losing a significant amount of energy.
- The baryonic gas on the other hand is collisional, and its short range interactions are very well described by the Standard Particle Model. During the galaxy cluster collision, the baryonic parts interact and they lose energy through particle collision. This interaction decouples the baryonic gas from the galaxies and dark matter, and, given that we can directly observe the hot gas (thanks to X-ray astronomy), we can measure the separation between the centroid of the hot gas and the centroid of the galaxies.

If there was no dark matter, then after the collision the weak lensing mapping of the mass distribution would be very close to the hot gas distribution, because the hot gas would be the dominant mass density in the cluster. If dark matter were to exists,

then it would dominate the mass density distribution in the galaxy cluster and the weak lensing mapping would be very similar to the galaxies distribution (because they are also collisionless).

What we observe in the Bullet Cluster is the latter case, in which hot gas decouples from dark matter and galaxies. By mapping the cluster components and measuring the difference between the centroids, it was concluded that there is a dark matter component in the clusters. Very accurate measurements and estimates of the centroids show a small collisional nature in the dark matter component, such measurements allows to estimate the *thermally averaged cross-section* of the dark matter particle ( $\langle \sigma v \rangle$ ). Therefore, it is worth exploring the collisional dark matter scenario.

## 1.2 Particle Dark Matter

So far when talking about dark matter we have talked about an astrophysics problem, however, this problem has also been tackled by the particle physics community. In quantum field theory, particles are modeled as an excitation of space-time fields, and their interactions as interference among those fields.

The first good candidate for a dark matter particle is the neutrino. It is a stable particle, and it does not experience electromagnetic or strong interaction[3]. From the measurements of the cosmic microwave background, it is possible to estimate the number of neutrinos that existed in thermal equilibrium during the early universe and the temperature at which they decoupled from the primordial plasma, allowing to define a *thermal relic density*, which is the density of neutrinos (or any specie) at the moment of the decoupling. From there, using general relativity, we can study

## 1.2. PARTICLE DARK MATTER

---

how this density affects the expansion of the universe and place limits on the mass of the particle[17]. All in all, the neutrino mass was too small to allow for the formation of the large scale structure of the universe. And so, the neutrino was eliminated as a candidate.

In order to form large scale structure in a dark matter dominated universe, the dark matter particle must decouple as a cold relic<sup>3</sup>. This constrain and the neutrino case (where there is weak and gravitational interaction) lead to the proposal of many *weakly interacting massive particles* (WIMPs) as dark matter particle candidates. These candidates have masses in the GeV regime and a cross section in the same order of magnitude as the weak interaction cross section. The fact that many extensions of the standard model offered WIMP particles with almost the same thermal relic density as the dark matter particle was known as the WIMP miracle.

There are many other candidates for a dark matter particle, but in the end, every candidate must reproduce the thermal relic density, allow for the formation of halos and large scale structure, and not interact with the electromagnetic field. Any interaction that the dark matter particle has (besides gravitational) implies a cross section  $\langle\sigma v\rangle$  thus making dark matter collisional. The thermally averaged cross-section  $\langle\sigma v\rangle$  can be measured using collisions of galaxy clusters such as the Bullet Cluster, once again motivating the study of collisional dark matter.

---

<sup>3</sup>A particle that decouples from the primordial plasma with a non-relativistic velocity.

## 1.3 The Boltzmann Equation

The Boltzmann equation was originally proposed in 1872 by Ludwig Boltzmann and is used to model the behavior of statistical systems outside of the equilibrium. Formally, the Boltzmann equation describes the evolution of the phase space of a typical dark matter particle, such that  $f(\mathbf{r}, \mathbf{v}, t)d\mathbf{r}d\mathbf{v}$  is the probability of finding the dark matter particle in a position between  $\mathbf{r}$  and  $\mathbf{r} + d\mathbf{r}$ , with velocity velocity between  $\mathbf{v}$  and  $\mathbf{v} + d\mathbf{v}$ . By multiplying the probability phase space by the mass of a dark matter particle and the number of particles enclosed in the volume of interest ( $n$ ), we can use the Boltzmann equation to describe the phase space mass density of a fluid, instead of the phase space probability of a single particle. In this work we are interested in the phase space mass density of a dark matter fluid, whose time evolution is described by the Boltzmann equation

$$\frac{\partial f}{\partial t} + \dot{\mathbf{x}} \frac{\partial f}{\partial \mathbf{x}} + \dot{\mathbf{v}} \frac{\partial f}{\partial \mathbf{v}} = C[f], \quad (1.4)$$

the left hand side is known as the Liouville operator and the right hand side is known as the *Collisional* operator. The Liouville operator represents the evolution of the system following classical mechanics, without considering short range interaction between particles (the collisions). The collisional operator is an integral operator that relates the possibility of a collision with the state of the system  $f(\mathbf{r}, \mathbf{v}, t)$ . In other words, the collisional operator quantifies the effect of the collisions in the phase space evolution. A complete modeling of the collisional operator requires knowledge of the short range interactions between particles, given that we do not know the short range interaction of a dark matter particle, we must work with approximation schemes. This is going to be expanded in section 1.5.

For a collisionless fluid, the Boltzmann equation becomes the Vlasov equation:

$$\frac{\partial f}{\partial t} + \dot{\mathbf{x}} \frac{\partial f}{\partial \mathbf{x}} + \dot{\mathbf{v}} \frac{\partial f}{\partial \mathbf{v}} = 0. \quad (1.5)$$

Which simply dictates that the phase space distribution function is constant along the trajectories of the system[1]

## 1.4 Lattice Boltzmann Method

The Lattice-Boltzmann method divides the phase space into a lattice and solving the Boltzmann equation in such lattice. In each cell of the lattice there is a density which represents the mass of fluid in the position and velocity range correspondent to the cell's location in the lattice. The main effect of the discretization of the phase space is that we no longer simulate the entire phase space, but a discrete number of velocities and positions, which allows for the use of integer arithmetic. The use of integer arithmetic introduces lattice noise but eliminates the floating point error. In the limit of high resolution, the absence of floating point error and the tendency of the lattice noise towards zero guarantees that the method converges to the continuum solution and makes it a Lagragian, Symplectic and conservative algorithm.

However, this method has one big drawback. The time evolution of the phase space is calculated using a direct integration scheme, which implies that for a simulation with  $N$  spatial dimensions each one having size  $n$ , we would need to store  $n^{2N}$  cell units per timestep. This is in fact a very heavy constrain because most cases of interest are three dimensional. For example, in a three dimensional distribution, if

the grid size were to be 64, then we would need almost 600 Gigabytes of memory just to store the lattice. The specifics of implementing a Lattice Boltzmann method are discussed further in section 2.1.

## 1.5 BGK Approximation

The main challenge when solving the Boltzmann equation is the collisional operator. Modeling a collisional operator and solving the subsequent integral is not a straightforward procedure, which is why simpler alternatives have been widely considered.

The Bhatnagar–Gross–Krook approximation was proposed in 1954 [18] in order to simplify the collision integral. The approximation operates under the assumption that the large amount of detail involved in the two-body interactions are not likely to significantly influence the macroscopic variables[19]. This is known as an mesoscopic approach, because we disregard the microscopic interactions while preserving the macroscopic properties of the system. The scheme ignores the specifics of the two-body interactions but keeps the tendency of the system towards local equilibrium and then global equilibrium.

Local equilibrium is defined by the following condition:

$$C[f_e] = 0. \tag{1.6}$$

Which simply states that in *local equilibrium*, the collisions do not affect the time derivative of the distribution function. Note that local equilibrium does not mean that the macroscopic variables of the system are constant in space and time, but

## 1.5. BGK APPROXIMATION

---

that the local value of  $f(\mathbf{r}, \mathbf{v}, t)$  corresponds to the local value of  $f_e(\mathbf{r}, \mathbf{v})$ , for an appropriate equilibrium distribution function  $f_e(\mathbf{r}, \mathbf{v})$ . Finally, the BGK operator can be stated as:

$$C[f] = -\frac{1}{\tau}(f(\mathbf{r}, \mathbf{v}, t) - f_e(\mathbf{r}, \mathbf{v})), \quad (1.7)$$

where  $\tau$  is a characteristic relaxation time for the system. In most cases, the equilibrium function obeys the Maxwell-Boltzmann distribution, however, Fermi-Dirac distributions were widely used in the early years of the Lattice Boltzmann methods. In recent years modified Maxwellians have been proposed to extend the BGK scheme to the quantum realm[20] and to include annihilation and creation of particles. The specifics of our implementation of the BGK approximation are discussed in section [2.2](#).

# Chapter 2

## The Lattice Boltzmann Algorithm

### 2.1 General Description

The heart of the Lattice-Boltzmann algorithm is the discretization of the phase space[1] [2].

To discretize the phase space, we must choose the region to simulate. In this work, we name the extremal values in the  $w$  axis of the phase space  $W_{min}$  and  $W_{max}$ . Then, one has to fix either the size of the grid or the size of the lattice. We name the size of the grid in the  $w$  axis  $N_w$  (i.e.  $N_x$  or  $N_{vz}$ ). The size of a lattice unit in the  $w$  axis (which we are going to name  $dw$ ) and the extremal values are related by

$$dw = \frac{W_{max} - W_{min}}{N_w}. \quad (2.1)$$

In this work use the phase space mass density, which means that  $f(\mathbf{r}, \mathbf{v}, t)d\mathbf{r}d\mathbf{v}$  is

## 2.1. GENERAL DESCRIPTION

---

the *mass* of dark matter whose position is between  $\mathbf{r}$  and  $\mathbf{r} + d\mathbf{r}$ , and its velocity is between  $\mathbf{v}$  and  $\mathbf{v} + d\mathbf{v}$ . Now that we have properly defined the grid, we must initialize the phase space. The initial conditions are discussed in detail in section 2.3.

After initialization, the phase space evolves by the action of the Louville operator and the Collisional operator. However, the collisions are modeled as instantaneous, which allows us to concentrate their entire influence in a single collisional step per time step. The schematics of the algorithm can be seen in figure 2.1.

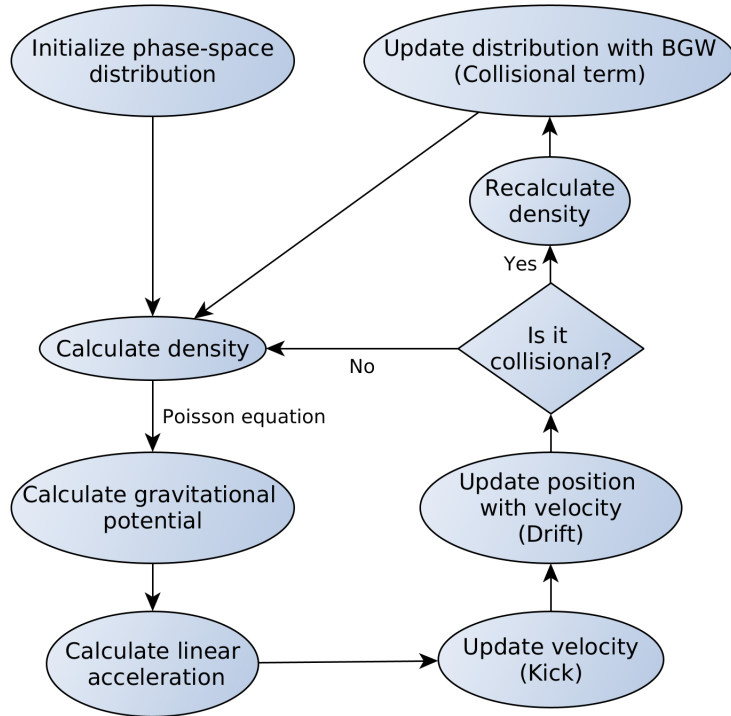


Figure 2.1: Flowchart of our lattice Boltzmann implementation.

After having initialized the phase space, we can obtain the spatial density of matter

by numerical integration in the velocity space

$$\rho(\mathbf{r}, t) = \int_{-\infty}^{\infty} f(\mathbf{r}, \mathbf{v}, t) d\mathbf{v}. \quad (2.2)$$

When evaluating in the lattice the integral becomes a sum over the entire velocity lattice

$$\rho(\mathbf{r}, t) = \sum_{\mathbf{v}_{min}}^{\mathbf{v}_{max}} f(\mathbf{r}, \mathbf{v}, t) d\mathbf{v}, \quad (2.3)$$

and during initialization

$$\rho(\mathbf{r}, 0) = \sum_{\mathbf{v}_{min}}^{\mathbf{v}_{max}} f(\mathbf{r}, \mathbf{v}, 0) d\mathbf{v}. \quad (2.4)$$

Once we have calculated the density, we solve the Poisson equation to obtain the potential due the gravitational interaction [1]

$$\nabla^2 \Phi(\mathbf{r}, t) = 4\pi G \rho(\mathbf{r}, t). \quad (2.5)$$

Where  $\Phi(\mathbf{r}, t)$  is the gravitational potential and  $G$  is the gravitational constant. To solve the Poisson equation we use the Fourier pseudo-spectral method, which allows for very fast numerical solutions by making use of the Fast Fourier Transform algorithm. We apply a Fast Fourier Transform (FFT) to the density, then solve the equation in the Fourier space, and then apply an inverse transform (IFFT). In the Fourier space the Poisson equation is given by[21] [22]

$$\lambda_{\mathbf{k}}^2 \hat{\Phi}(\mathbf{k}, t) = 4\pi G \hat{\rho}(\mathbf{k}, t). \quad (2.6)$$

Where  $\hat{\rho}(\mathbf{k}, t)$  is the Fourier transform of  $\rho(\mathbf{r}, t)$ , and  $\lambda_{\mathbf{k}}$  is a constant that depends

## 2.1. GENERAL DESCRIPTION

---

on the size of the lattice and the wave vector  $\mathbf{k}$ .  $\lambda_{\mathbf{k}}$  is calculated according to the approximation scheme used to solve the equation. In the the pseudo-spectral approximation,  $\lambda_{\mathbf{k}}$  is given by

$$\lambda_{\mathbf{k}}^2 = - \left( \frac{2\pi k_x}{X_{max} - X_{min}} \right)^2 + \left( \frac{2\pi k_y}{Y_{max} - Y_{min}} \right)^2 + \left( \frac{2\pi k_z}{Z_{max} - Z_{min}} \right)^2. \quad (2.7)$$

Therefore, solving the Poisson equation in the Fourier space is reduced to simple arithmetic. Thanks to the highly efficient implementations of the Fast Fourier Transform Algorithm available nowadays, solving the Poisson equation takes very little time and computational resources. In this work we use the Fastest Fourier Transform of the West[23] subroutine to handle the Fast Fourier Transforms.

Afterwards we compute the acceleration

$$\mathbf{a}(\mathbf{r}, t) = -\nabla\Phi(\mathbf{r}, t). \quad (2.8)$$

We use a central difference numerical derivative in our implementation.

Now, in order to update the phase space, we must first define the time interval to simulate: we name  $N_t$  the number of time *instants* to simulate and  $dt$  the length of each of such instants. After calculating the acceleration and defining  $dt$ , we can update our phase space. As mentioned in section 1.4, the subtlety here is that we will only use integer arithmetic, which means that we do not exactly care about the change in velocity during a time  $dt$ , but for how many cells in the phase space lattice that change represents. This is modeled by

$$\mathbf{v}_{n+1} = \mathbf{v}_n + [\mathbf{a}_n dt]. \quad (2.9)$$

With  $\lfloor x \rfloor$  representing the operator “to nearest integer”, so that  $\mathbf{v}$  and  $\lfloor \mathbf{ad}t \rfloor$  are vectors of integers and  $n$  represents the time instant. The update of the velocity is known as “kick”. Analogously, the update of the position is known as “drift”, and is given by

$$\mathbf{r}_{n+1} = \mathbf{r}_n + \lfloor \mathbf{v}_n dt \rfloor. \quad (2.10)$$

The use of only integer arithmetics allows for the elimination of the rounding error but introduces lattice noise. Regardless, this method creates a one to one map with the continuous solution [1] [2].

The “kick” and “drift” together are known as the “Streaming” step, and it represents the classical movement of particles under a potential but without considering the collision of particles. In a collisionless simulation we can just calculate again the density and continue the algorithm from there. For a collisional simulation, we must define a collisional step.

## 2.2 The Collisional Step

Solving the collisional integral  $C[f]$  is not a straight-forward task, as it depends on the modeling of the short range interactions that we decide to assign to the dark matter particle. Given that the short range interactions of dark matter are unknown, we avoid using a specific description of the microscopic interactions and choose to use a mesoscopic approach instead, as discussed in section 1.5. The BGK collisional operator is given by

$$C[f] = -\frac{1}{\tau}(f(\mathbf{r}, \mathbf{v}, t) - f_e(\mathbf{r}, \mathbf{v})), \quad (2.11)$$

## 2.2. THE COLLISIONAL STEP

---

which in the context of the direct integration scheme used in the simulation becomes

$$f(\mathbf{r} + \mathbf{v}dt, \mathbf{v}, t) = f(\mathbf{r}, \mathbf{v}, t) - \frac{dt}{\tau}(f(\mathbf{r}, \mathbf{v}, t) - f_e(\mathbf{r}, \mathbf{v})). \quad (2.12)$$

The idea behind this approach is to recover the macroscopic properties of the fluid without committing to a particular microscopic description. In this scenario, the macroscopic effects of the collisions is a local relaxation towards equilibrium, which the BKG operator models using a relaxation time  $\tau$  and a local equilibrium distribution  $f_e(\mathbf{r}, \mathbf{v})$ .

We implement the collisional operator as a collisional step after the streaming step, in which the system performs a relaxation with characteristic (relaxation) time  $\tau$  towards the local equilibrium distribution  $f_e(\mathbf{r}, \mathbf{v})$ . It is important to note that the BGK collisional operator is a *scattering* operator and does not consider annihilation or creation of particles.

After defining the collisional term, we have to choose a distribution function  $f_e(\mathbf{r}, \mathbf{v})$ . We claim that the phase space distribution relaxes towards local equilibrium, which means a displacement in the phase space and not the introduction or annihilation of mass. Therefore, the equilibrium distribution must be perfectly *normalized* in order to enforce particle number conservation. We normalize the equilibrium distribution by using macroscopic quantities obtained through numerical integration of the velocity part of the phase space. This macroscopic quantities are: the spatial density  $\rho(\mathbf{r}, t)$ , the macroscopic velocity  $\mathbf{u}(\mathbf{r}, \mathbf{v})$  and the internal energy  $e(\mathbf{r}, \mathbf{v})$ .

The volumetric density is the same density we have been using so far defined by the

integral of equation 2.2. The macroscopic velocity  $\mathbf{u}(\mathbf{r}, \mathbf{v})$  is defined by the integral

$$\mathbf{u}(\mathbf{r}, \mathbf{v}) = \int_{-\infty}^{\infty} f(\mathbf{r}, \mathbf{v}, t) \mathbf{v} d\mathbf{v}, \quad (2.13)$$

when evaluating in the lattice the integral becomes

$$\mathbf{u} = \sum_{\mathbf{v}_{min}}^{\mathbf{v}_{max}} f(\mathbf{r}, \mathbf{v}, t) \mathbf{v} d\mathbf{v}. \quad (2.14)$$

The internal energy is defined by the integral

$$e(\mathbf{r}, \mathbf{v}) = \frac{1}{2} \int_{-\infty}^{\infty} f(\mathbf{r}, \mathbf{v}, t) (\mathbf{v} - \mathbf{u})^2 d\mathbf{v}. \quad (2.15)$$

Which also becomes a sum when evaluating in the lattice

$$e(\mathbf{r}, \mathbf{v}) = \frac{1}{2} \sum_{\mathbf{v}_{min}}^{\mathbf{v}_{max}} f(\mathbf{r}, \mathbf{v}, t) (\mathbf{v} - \mathbf{u})^2 d\mathbf{v}. \quad (2.16)$$

Note that we are not including explicitly the mass of the dark matter particle in this integrals because it has already been included in the definition of the phase space.

Now that we have well defined macroscopic variables, we can proceed to choose an equilibrium distribution. Such distribution must obey the following condition

$$C[f_e] = 0. \quad (2.17)$$

Which simply means that if the system is already in local equilibrium, then there is no relaxation. This condition can also be stated as “the equilibrium function must be

## 2.2. THE COLLISIONAL STEP

---

a collisional invariant". In order for  $f_e(\mathbf{r}, \mathbf{v})$  to be a collisional invariant, it must be built with variables that are also collisional invariant. Fortunately, the macroscopic variables already defined in this chapter are also collisional invariants, and so, we can use them to build equilibrium distributions. The idea behind normalization is to obtain the same macroscopic variables when integrating over  $f_e(\mathbf{r}, \mathbf{v})$  instead of  $f(\mathbf{r}, \mathbf{v}, t)$ . In this work we use distributions based on the Maxwell-Boltzmann velocity distribution. Alternative equilibrium distributions functions can be considered and may be of interest, but they are beyond the scope of this work. In particular, quantum Maxwellians may be used to include annihilation and creation of particles, and the effects of Bose-Einstein, Fermi-Dirac statistics[20].

The equilibrium function to use is a classical Maxwellian properly normalized for the case of interest

$$f_e(\mathbf{r}, \mathbf{v}) = \frac{\rho}{[2\pi e(\mathbf{r}, \mathbf{v})]^{D/2}} \exp\left[-\frac{(\mathbf{v} - \mathbf{u})^2}{2 e(\mathbf{r}, \mathbf{v})}\right]. \quad (2.18)$$

Where  $D$  is the number of spatial dimensions. For example, if the system is a three dimensional dark matter halo, then  $D$  will be equal to three. The Maxwell distribution was originally used to describe the probability distribution of the velocity in a gas under kinetic theory assumptions. Here, we assume collisions as a phenomena that happens instantly. During the time in between, the mechanics of the system are governed by the self-gravitational potential. Therefore, the Maxwell distribution is a good ansatz for the collisional equilibrium distribution function  $f_e(\mathbf{r}, \mathbf{v})$ .

Finally, the only thing left to choose is a relaxation time. As in classic kinetic theory, our relaxation time will be given by

$$\tau = \frac{1}{n\langle\sigma v\rangle}. \quad (2.19)$$

In terms of the matter density instead of particle number it becomes

$$\tau = \frac{m}{\rho \langle \sigma v \rangle}, \quad (2.20)$$

with  $n$  being the mean particle number in the halo,  $m$  being the mass of a dark matter particle,  $\rho$  being the average density of a dark matter halo and  $\langle \sigma v \rangle$  is the thermally averaged cross-section of the particle.

For this simulation we use the average *matter* density of the universe, given by the most recent results of the Planck probe[24]. We are also going to use the value of  $\langle \sigma v \rangle$  constrained by the Bullet Cluster data [25] [26], and for the dark particle mass we are going to use the lowest mass possible for a fermionic dark matter particle candidate [15]. These values are:

$$m = 0.7 \text{ KeV} \quad (2.21)$$

$$\langle \sigma v \rangle = 3 \times 10^{-26} \text{ cm}^3/\text{s} \quad (2.22)$$

$$\rho = \Omega_m = 0.312 \quad (2.23)$$

The final value of  $\tau$  will depend on the particular set of units used in every scenario. Alternative set of values may be used to test dark matter particle candidates.

### 2.2.1 Parameters of the simulation

There are still a few important aspects of the simulation still to be defined: the units, the boundary conditions and the grid parameters.

To set the units we fix the value of one spatial unit ( $us$ ), one unit of time ( $ut$ ), and

## 2.2. THE COLLISIONAL STEP

---

one unit of mass ( $um$ ) of the simulation, and from there, we proceed to calculate the values of the physical constants in our units. The physical constants of interest here are the gravitational constant, and the relaxation time  $\tau$  used in the collisional step. We chose units to simulate a dark matter halo of dimensions akin to the halo of some galaxies of the Local Group. Because of stability conditions, the units may differ between runs. The complete set of units used in the work is presented in the following table, where we use  $t_0$  to represent the age of the universe:

No. of axes	1 us [kpc]	1 ut [ $t_0$ ]	1 um [ $10^{11} M_\odot$ ]	$\tau$ [ut]
2	35	0.004	1	8972
4	50	0.003	1	11963
6	35	0.004	1	8972

For the boundaries we implement the following conditions:

- The boundaries of the spatial axes are periodic. Any portion of mass that leaves the distribution, will re enter through the opposite extreme. This condition assumes the system as periodic.
- Every portion of mass that leaves the distribution through the velocity axes will be lost forever. That means that if a particle has a velocity higher than the extremal values of the simulation, the particles is no longer considered in the next time step. This condition is not very limiting because we have high extremal values for the velocity and dark matter is traditionally modeled as *cold* or *warm*.

To set the grid parameters we must know how much memory is available. Increasing the number of dimensions increases also the amount of memory used to save the lattice, and therefore, reduces the size of the grid. In the following table we present

the values that characterize the grids used in this work:

No. of axes	$W_{min}$ [us]	$W_{max}$ [us]	$N_w$	$dw$ [1/us]	$dt$ [ut]
2	-1	1	2048	1/1024	0.4
4	-1	1	128	1/64	0.5
6	-1	1	32	1/16	0.5

We always use grid sizes in the form  $2^n$  with  $n$  positive integer, because the Fast Fourier Transform algorithm performs better and faster when calculating discrete transforms of sizes  $2^n 3^m 5^l$  for  $n, m, l$  positive integers.

## 2.3 Initial Conditions

We made use of different initial conditions depending on the objective of each run of the simulation. For the two dimensional phase space we had three initial conditions: Gaussian distribution, Jeans instability and Bullet Cluster-like scenario. For the four and six dimensional phase space we only used Gaussian initial conditions.

The Gaussian initial conditions are given by

$$f(\mathbf{r}, \mathbf{v}, 0) = A \exp\left(-\frac{\mathbf{r}^2}{\sigma_r^2} - \frac{\mathbf{v}^2}{\sigma_v^2}\right). \quad (2.24)$$

Where  $f(\mathbf{r}, \mathbf{v}, 0)$  is the initialization of the phase space density,  $A$  is an indirect measure of the total mass in the system, and  $\sigma_i$  are a measure of the width of the Gaussian profile in the given axis. Note that we use a single width for the spatial axes ( $\sigma_r$ ) and a single width for the velocity axes ( $\sigma_v$ ). The specific values for the parameters are presented in the following table:

### 2.3. INITIAL CONDITIONS

---

No. of axes	A	$\sigma_r$ [us]	$\sigma_v$ [us/ut]	Total mass [ $10^{10} M_\odot$ ]
2	$40 \text{ um us}^{-1} (\text{us/ut})^{-1}$	0.06	0.06	0.9
4	$50 \text{ um us}^{-2} (\text{us/ut})^{-2}$	0.2	0.2	7.8
6	$80 \text{ um us}^{-3} (\text{us/ut})^{-3}$	0.1	0.1	1.98

The total mass of the two dimensional run is in accordance with recent estimates of the total mass of the Small Magellanic Cloud [27]. Likewise, the four dimensional case is similar in total mass to the Triangulum Galaxy(M 33)[28] , and the six dimensional case is also similar to the Small Magellanic Cloud.

The Jeans instability initial conditions are given by

$$f(r, v, 0) = \frac{\bar{\rho}}{(2\pi\sigma^2)^{1/2}} \exp\left(-\frac{v^2}{2\sigma^2}\right) (1 + A \cos(kr)). \quad (2.25)$$

Such that  $\bar{\rho}$  is the average phase density of the system,  $\sigma^2$  is the variance of the velocity Gaussian profile,  $A$  is the amplitude of the density fluctuation and  $k$  is the wave number of the density fluctuation. The values used were:

$$\bar{\rho} = 10 \text{ um us}^{-1} (\text{us/ut})^{-1} \quad (2.26)$$

$$\sigma = 0.1 \text{ us/ut} \quad (2.27)$$

$$A = 0.9999 \quad (2.28)$$

$$k = 2\pi \text{ us}^{-1} \quad (2.29)$$

And last, the Bullet Cluster-like scenario, in which two Gaussian distributions collide due to their gravitational interaction, each Gaussian having its own variance and amplitude. In the real Bullet Cluster one of the clusters was heavier than the other, therefore, we fix one halo heavier in our simulation.

The initial conditions are given by the function:

$$f(\mathbf{r}, \mathbf{v}, 0) = A_1 \exp\left\{-\frac{(x - 0.4)^2}{2\sigma_1^2} - \frac{v^2}{2\sigma_v^2}\right\} + A_2 \exp\left\{-\frac{(x + 0.4)^2}{2\sigma_2^2} - \frac{v^2}{2\sigma_v^2}\right\}. \quad (2.30)$$

Here  $A_i$  is a measure of the total mass of the  $i$ th halo,  $\sigma_i^2$  is the variance of the Gaussian profile of the halo in the spatial axis, and  $\sigma_v^2$  is the variance of the Gaussian profile in the velocity axis. The values used to initialize the simulation were:

$$\sigma_1 = 0.04 \text{ us} \quad (2.31)$$

$$\sigma_2 = 0.04 \text{ us} \quad (2.32)$$

$$\sigma_v = 0.06 \text{ us} \quad (2.33)$$

$$A_1 = 40 \text{ um} \quad (2.34)$$

$$A_2 = 30 \text{ um} \quad (2.35)$$

# Chapter 3

## Numerical Tests

In order to test the code we ran a few numerical tests using the Gaussian and the Jeans instability initial conditions.

### 3.1 Two dimensional phase space

We begin with the Gaussian initial conditions because their simplicity and ease to analyze makes them the best introductory example. The Gaussian initialization can be seen in figure 3.1, along with its correspondent spatial density. After initialization, we proceed to calculate the potential and the acceleration, which can be seen in figure 3.2.

We reproduced previous work on the collisionless case done by Philip Mocz and Sauro Succi in 2016 [1] and Sebastian Franco in 2017 [2]. For it, we ran a collisionless

simulation and checked upon the behavior of the phase space density, the spatial density, the potential and the acceleration. In the phase space grid, we observed that the cells with positive velocity moved to the right side of the plot, but, as they moved to the right they were also being attracted towards the left because of the symmetry of the initial conditions. Therefore, the cells with positive velocity moved towards the inferior-right side of the plot, while cells with negative velocity moved towards the upper left side of the phase space.

The observed behavior was in complete accordance with previous work and can be seen in figure 3.3, where we plot different time instants chosen to display the clockwise spiral of the phase space evolution.

To visualize the linear density, we plot density vs position. We observed an initial increase in the height of the central peak and then little bumps trying to abandon the central distribution as they are gravitationally pulled back before crossing the spatial boundaries of the lattice. The bumps are simply the tails of the velocity distribution. This behavior can be seen in figure 3.4

We also reproduced the Jeans instability initial conditions. The parameters of the initialization were chosen to meet the Jeans instability criteria, in which the halos do not collapse but interchange mass with its neighbors. Each halo also behaves as a clockwise rotating spiral (which is not a surprise given that we used Gaussian initialization for the velocity). This results was also compatible with previous work. The evolution of the Jeans instability phase space can be seen in figure 3.5.

### 3.1. TWO DIMENSIONAL PHASE SPACE

---

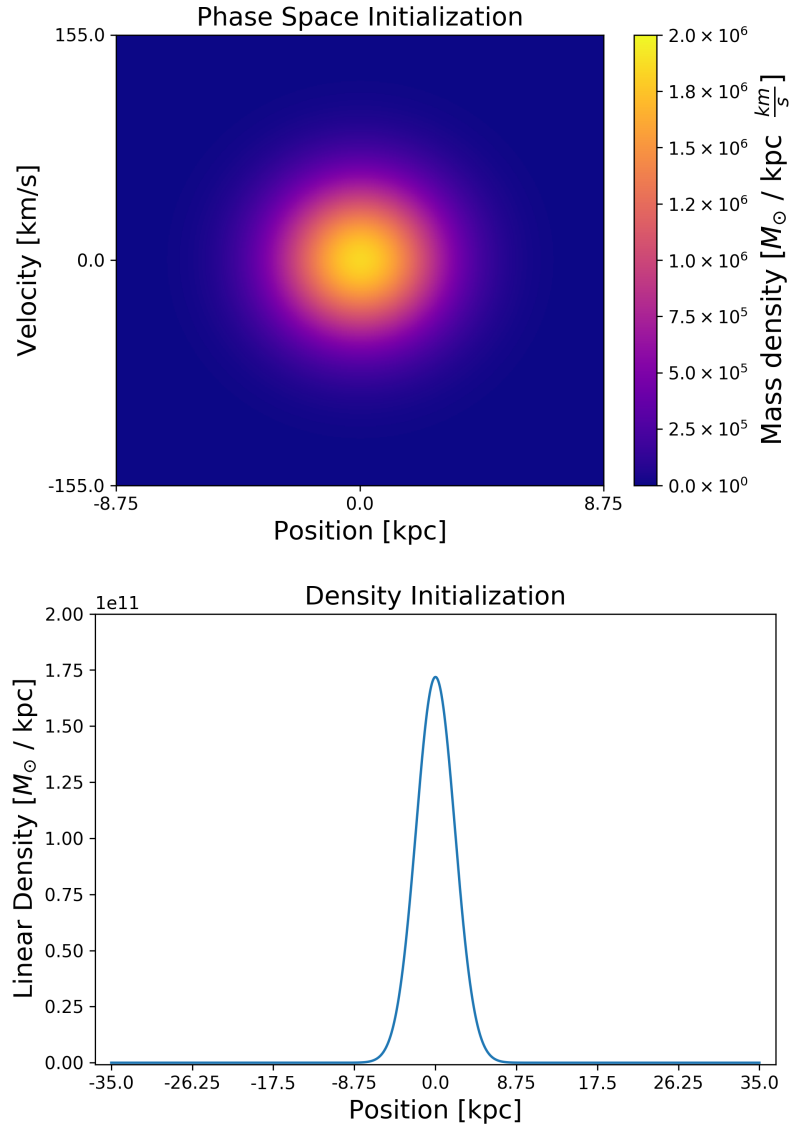


Figure 3.1: Up: initialization of the phase space. Position is represented in the  $x$  axis, and velocity in the  $y$  axis of the plot. Down: the spatial density obtained through integration.

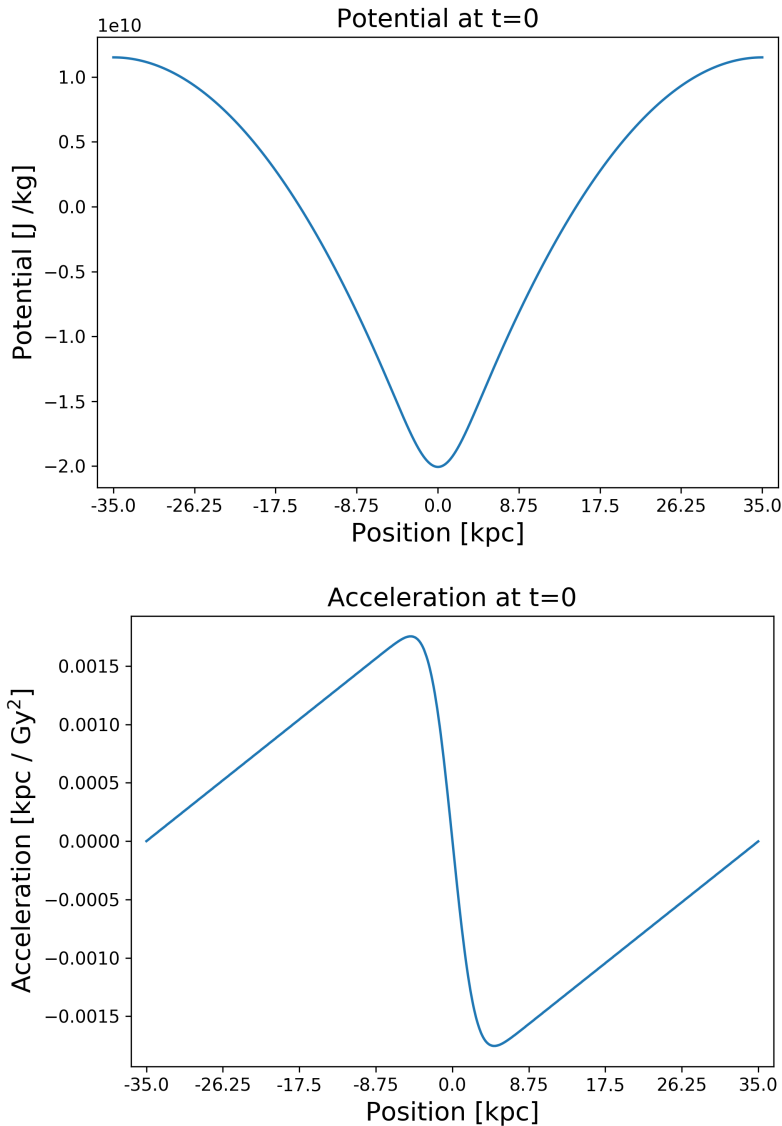


Figure 3.2: Up: The potential obtained by solving the Poisson equation. Given that the density was a Gaussian profile, it is no surprise that the potential is a negative Gaussian profile. Down: The acceleration obtain by numerical derivation of the potential.

### 3.1. TWO DIMENSIONAL PHASE SPACE

---

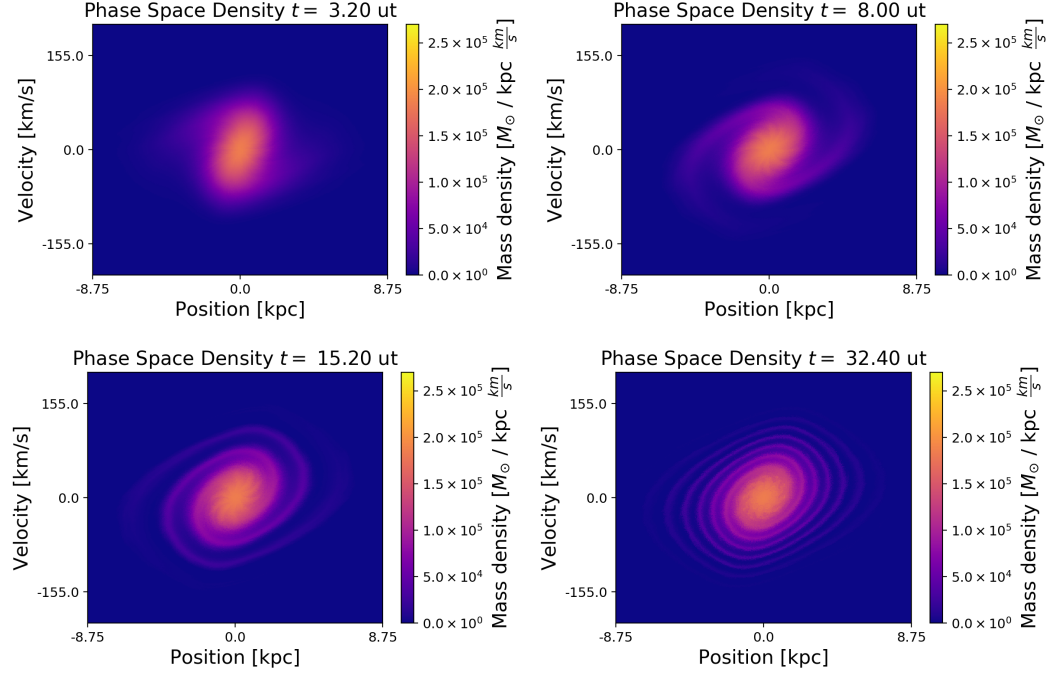


Figure 3.3: Upper left: Phase space 154 million years after initialization. Upper right: Phase space 484 million years after initialization. Bottom left: Phase space 881 million years after initialization. Bottom right: Phase space 1983 million years after initialization. It is evident that the phase space behaves as a clockwise rotating spiral.

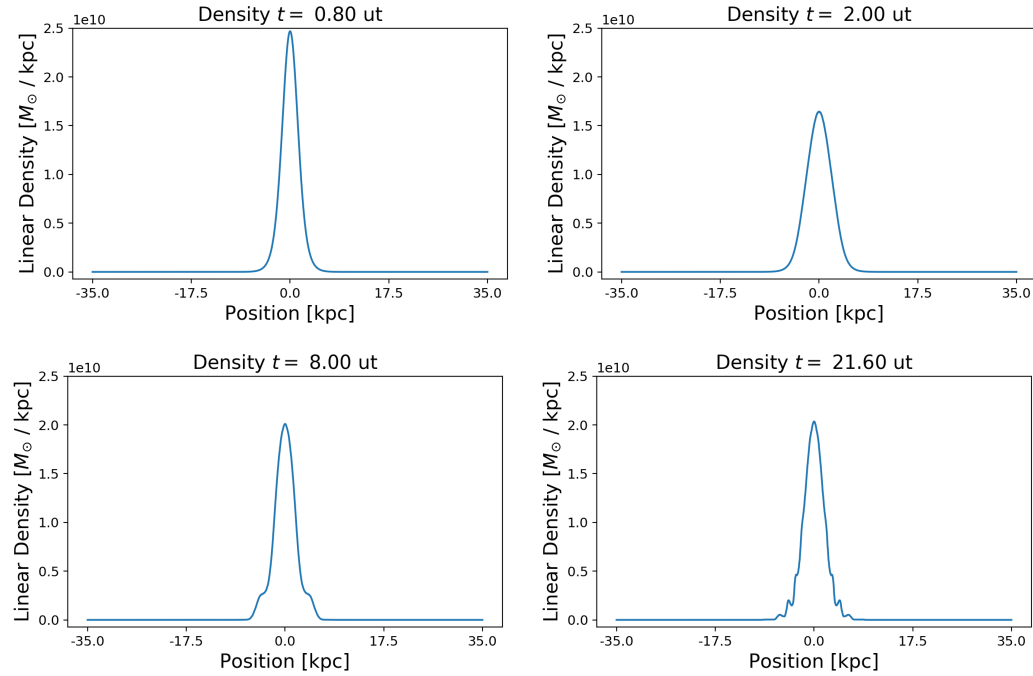


Figure 3.4: Upper left: linear density with its central peak at maximum height. Upper right: linear density with its peak at a local minima after having reached maximum height . Bottom left: little bumps can be seen at the tails of the distribution. Bottom right: the tails of the distribution are completely bumpy. These bumps are the same arms observed in the phase space.

### 3.1. TWO DIMENSIONAL PHASE SPACE

---

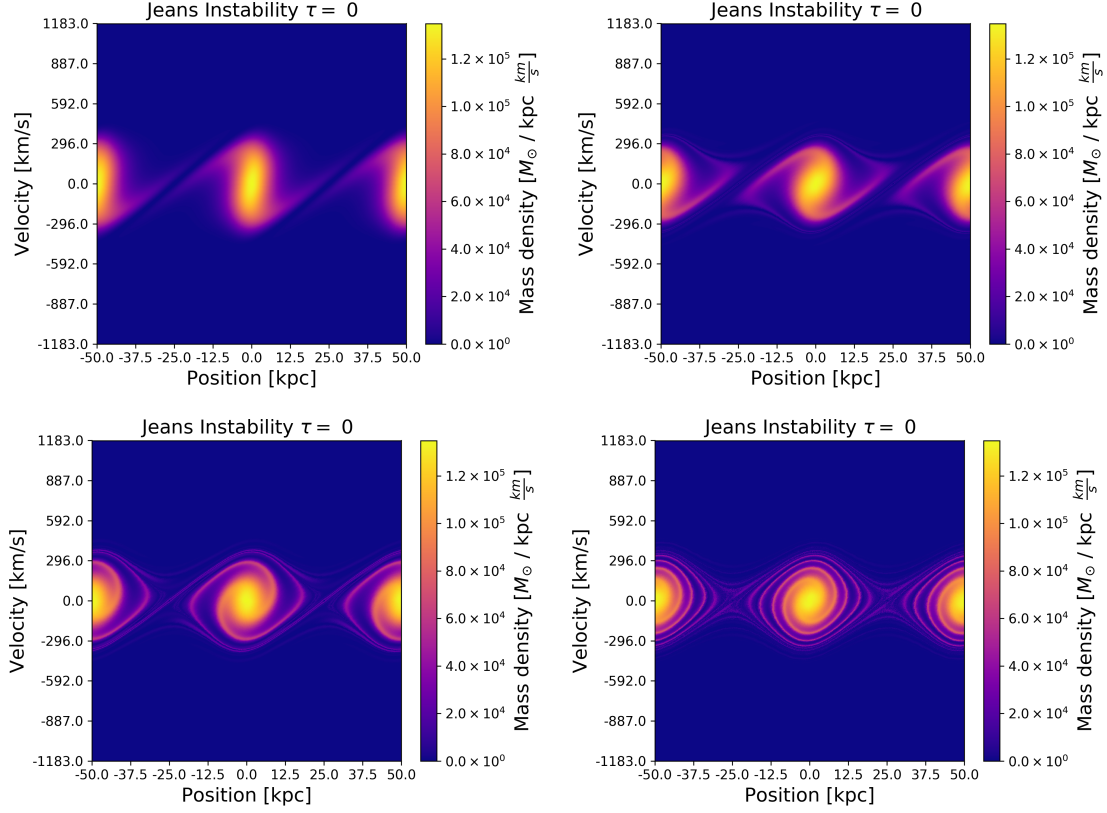


Figure 3.5: Upper left: Phase space 72 million years after initialization. Upper right: Phase space 227 million years after initialization. Bottom left: Phase space 413 million years after initialization. Bottom right: Phase space 930 million years after initialization. The behavior is the same as three successive Gaussian conditions.

## 3.2 Four dimensional phase space

In the four dimensional phase space, we made use only of the Gaussian initial conditions. Our main interest here is once again to test the code, and also to study the effects of a time step chosen too small.

The initialization of the Gaussian conditions can be seen in figure 3.6. Here we plot a 2D cut of the four dimensional phase space. We take the cut  $f(x, y = 0, vx, vy = 0)$  because is a direct analog of the phase space we saw in last section. We also plot the potential of the system, and the spatial density along with the correspondent acceleration vector field.

Let's consider first the two dimensional spatial density. The distribution initially collapses very quickly and then emits little bumps of matter. However, once again, the bumps are gravitationally pulled back before leaving the boundaries of the simulation. This behavior is completely equivalent to the one dimensional spatial density from last section. The spatial density can be observed in figure 3.7.

To analyze the phase space we plot a two dimensional cut of it. In figure 3.8 we can see the evolution of a central cut of the phase space. Once again, we see the phase space forming a clockwise spiral. Nonetheless, due to the low resolution, the arms are not well defined after a long time, this is the same effect the makes the density bumps invisible in figure 3.7.

Due to the discretization, we must be careful when choosing the size of the time step ( $dt$ ). If we choose it too small, it will be shorter than the time the *information* needs to propagate in the lattice. When this happens, we will see sections of the phase

### 3.2. FOUR DIMENSIONAL PHASE SPACE

---

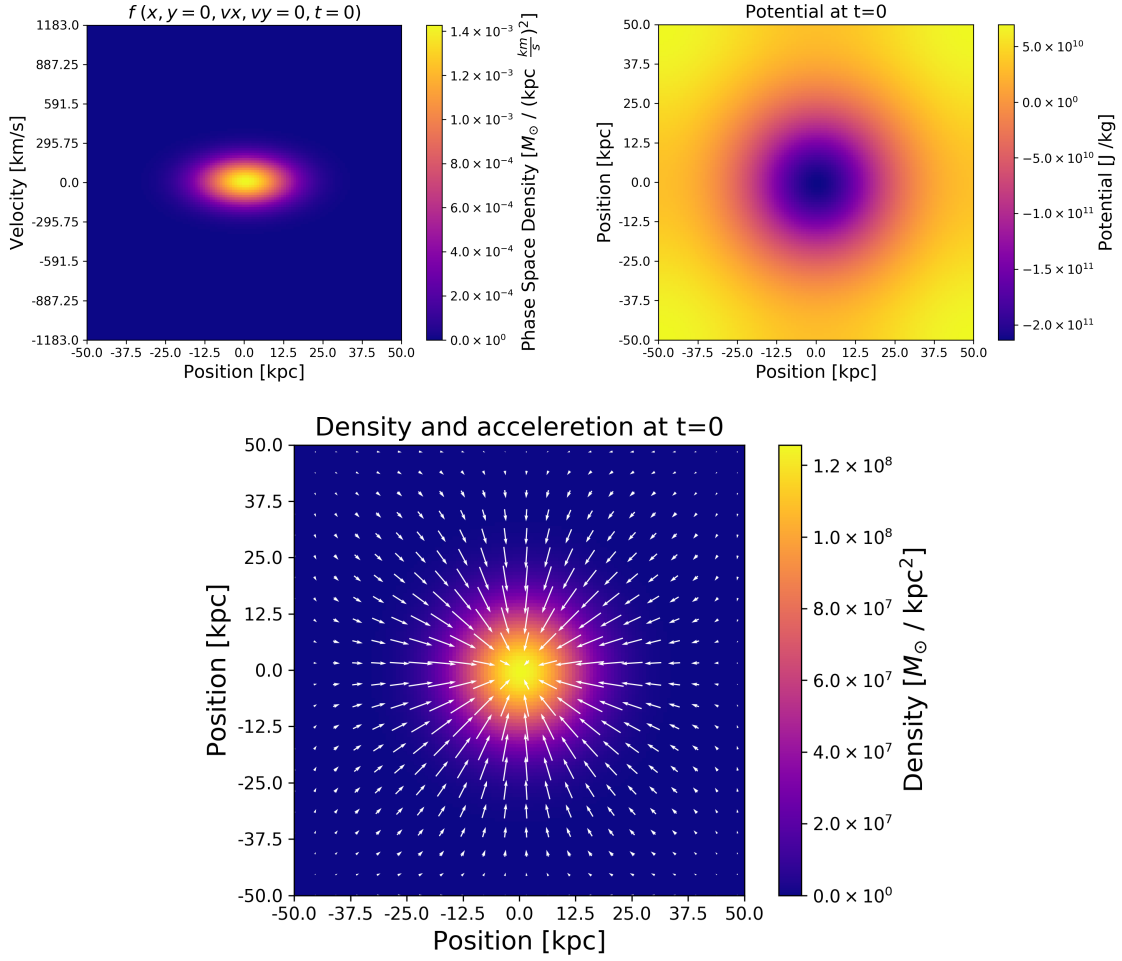


Figure 3.6: Upper left: the cut  $f(x, y = 0, vx, vy = 0)$  at  $t = 0$  of the phase space. It is equivalent to the initial Gaussian conditions from last section. Upper right: the potential due initial conditions, it is a bidimensional version of the potential of last section. Bottom: the density from initialization along with the acceleration vector field (white arrows). Initially the system is accelerating towards its centre.

space completely frozen in time until information has had enough time to propagate. If we choose a time step too big, the time integration will diverge from the real solution because of the direct integration scheme used. The effect of a poorly chosen time step can be appreciated in figure 3.9, where we have chosen the time step to be

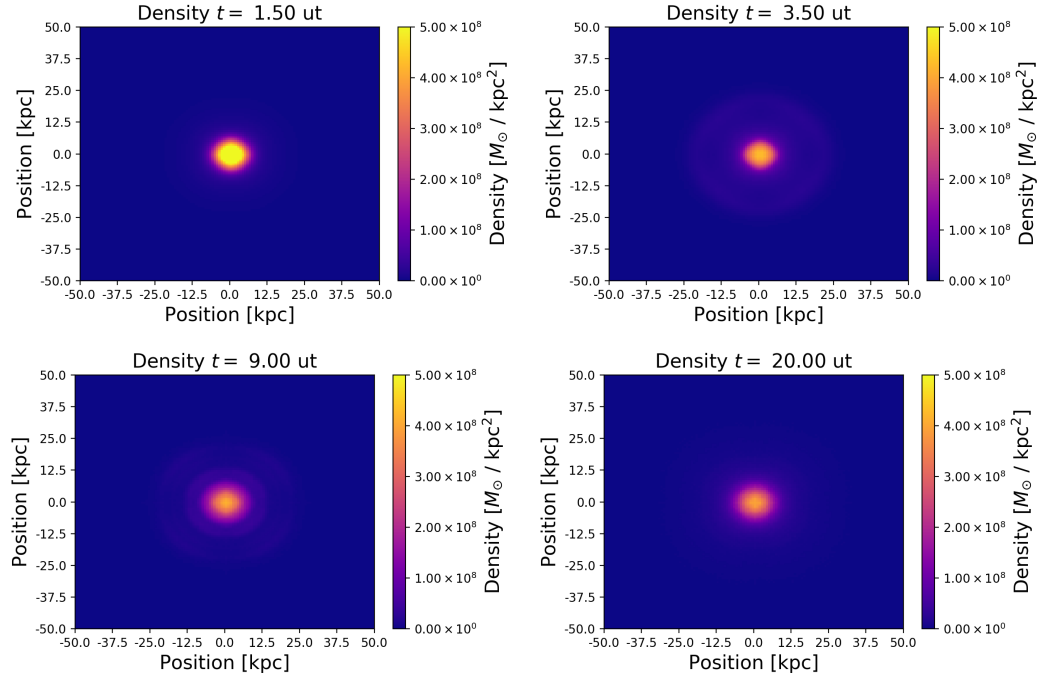


Figure 3.7: Upper left: density at  $t = 1.5$  ut, the instant of the initial collapse, note that this frame has a higher color scale. Upper right: density at  $t=3.5$  ut, here we observe the first bump of matter being expelled from the halo. Bottom left: now the spatial density multiple bumps of matter, these bumps are being gravitationally pulled back and lose intensity as they propagate. Bottom right: the bumps are now invisible at this color scale but the distribution is still bumpy.

0.1 ut, that is one forth of its previous value. In order to guarantee that the time step is big enough, it should be bigger than  $\frac{1}{3} \frac{\text{d}x}{\text{d}v}$ .

### 3.2. FOUR DIMENSIONAL PHASE SPACE

---

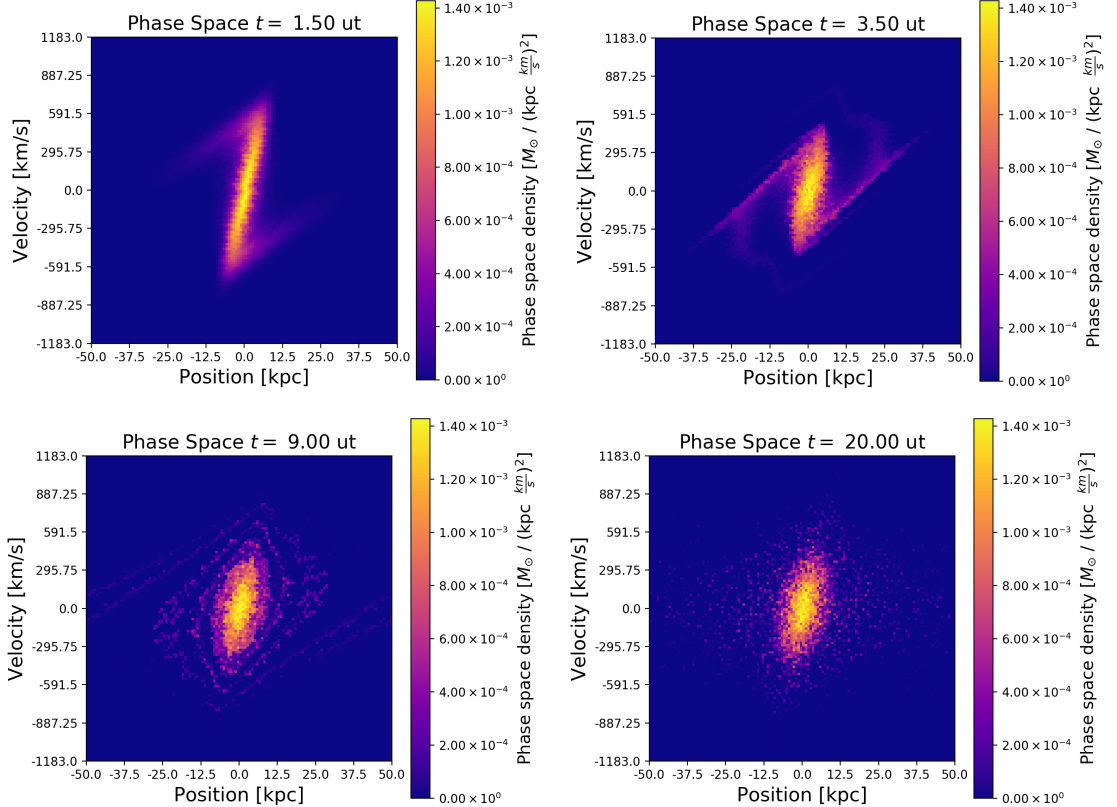


Figure 3.8: Upper left: phase space at  $t = 1.5$ , here the phase space is starting to form its characteristic clockwise rotating spiral. Upper right. The system keeps evolving into the spiral, note that there are no regions behaving as a single pixel. Bottom left: after a while the distribution forms the arms which characterize the bumps seen in figure 3.7. Bottom right: due the low resolution, the arm structure can no longer be distinguished.

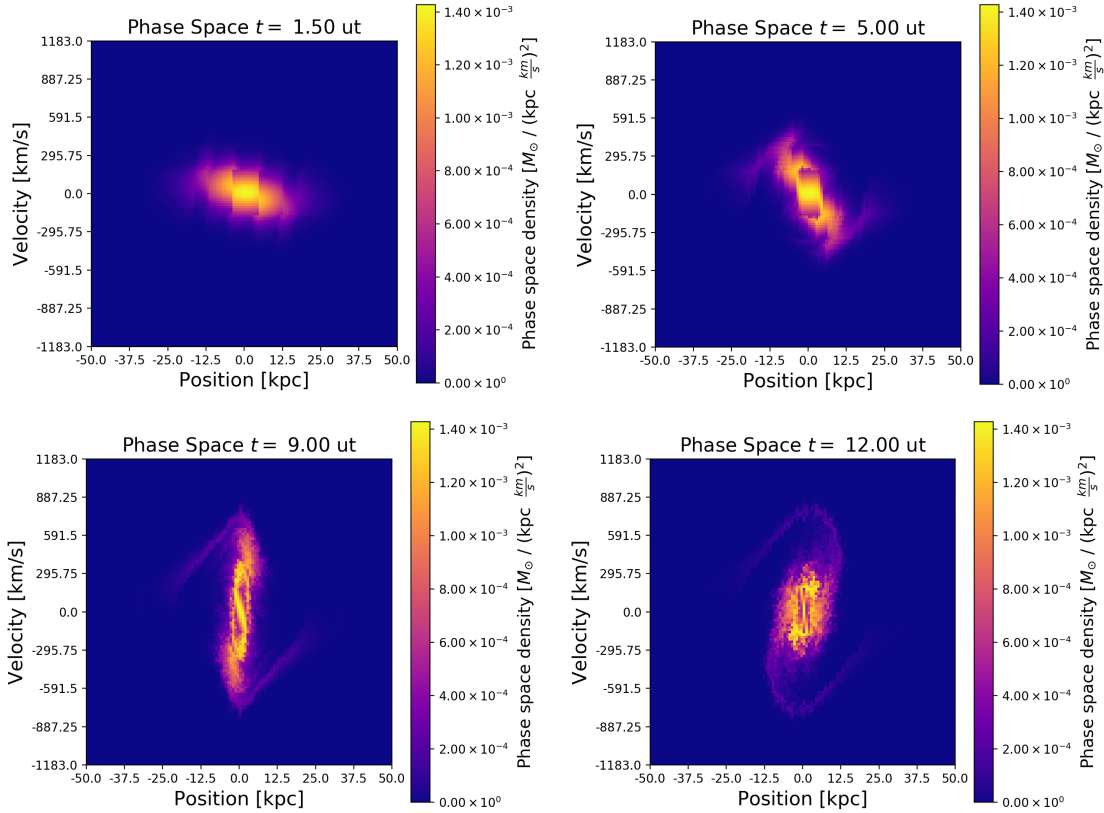


Figure 3.9: The evolution of the phase space when the time step is poorly chosen. The phase space is divided in regions that only update every few time steps. In the upper left frame we can see the initial segmentation of the distribution. Upper right: the divided phase space is trying to form its traditional clockwise spiral. Bottom left: the regions have changed internally, nonetheless the interface of the regions has a lasting influence on the distribution. Bottom right: the phase space spiral. This solution of the phase space is inaccurate because of the error introduced by the pixeling of the distribution.

### 3.3 Six dimensional phase space

We tested the six dimensional code using Gaussian conditions. However, the high dimensionality of the problem implies a very low resolution for the lattice, in order to comply to memory constraints. This low resolution carries along heavy visualization problems and a very high lattice noise. With such low resolution, we can not claim that the simulation is indeed recovering the continuum Boltzmann equation. More optimization is needed in order to obtain viable results from the six dimensional case. However, we will include some figures to illustrate the visualization in this run and how we know that the simulation is numerically unstable.

The simulation treats the phase space density of a cell in the lattice as a *Double-precision floating-point* number, which in the end means that each lattice cell occupies 8 bytes of memory space, and the whole lattice occupies  $8N_w^6$  bytes of memory. In the case of the six dimensional phase space, the memory requirement of the simulation is given by:

$$M = 2.5(8N_w^6) \quad (3.1)$$

We multiplied the size of the phase space grid in memory by 2.5 in order to account for the multiple lattices used in the simulation.

We initialized the phase space using a Gaussian distribution with the following parameters:

$$\sigma_r = 0.1 \text{ us} \quad (3.2)$$

$$\sigma_v = 0.1 \text{ us/ut} \quad (3.3)$$

$$A = 80 \text{ um} \quad (3.4)$$

Which yields a total mass of  $1.98 \times 10^{10} M_{\odot}$ , a value similar to the mass of the Small Magellanic Cloud [27]

We plot the central cut  $\rho(x, y, z = 0)$  of the density in figure 3.11, and the cut  $f(\mathbf{r}, \mathbf{v}, t)(x, y = 0, z = 0, vx, vy = 0, vz = 0)$  of the phase space in figure 3.10.

In the cut of the phase space we can see that initially, the phase space tries to form its typical clockwise rotating spiral, but the low resolution quickly introduces too much noise and the arm structure can no longer be resolved. This is a critical problem, because the lattice cells are now moving accordingly to the lattice noise instead of the real physics involved. The low resolution also carries along a big error when integrating the lattice to obtain the density (or any other macroscopic quantity).

In the cut of the density, we appreciate the same structure as in figure 3.7, nonetheless, we observe that there is a cross in the last two frames, this cross comes from the numerical error when integrating on the lattice, and has no physical meaning since we should be appreciating a circle.

In the collisional case the lattice noise introduced by the low resolution (exemplified by the crosses of figure 3.11) makes the normalization of the equilibrium function impossible, since the integral will differ considerably from its real value. The stability of the collisional step is very frail, as it depends strongly on the correct normalization of the equilibrium function and the simulation. Overall, the collisional simulation became unstable and we could not obtain results from it.

The easiest way to solve this is to exploit the symmetry of the initial conditions and only define half the lattice points per axis. This would dramatically reduce the memory requirement but will limit heavily the initial conditions to use. For

### 3.3. SIX DIMENSIONAL PHASE SPACE

---

example, we would not be able to run the Bullet Cluster-like conditions from section 4.1. A more formal approach involves parallelizing the simulation, in particular the integration over the velocity space and the update of the lattice. Regardless, both approaches are beyond the scope of this work.

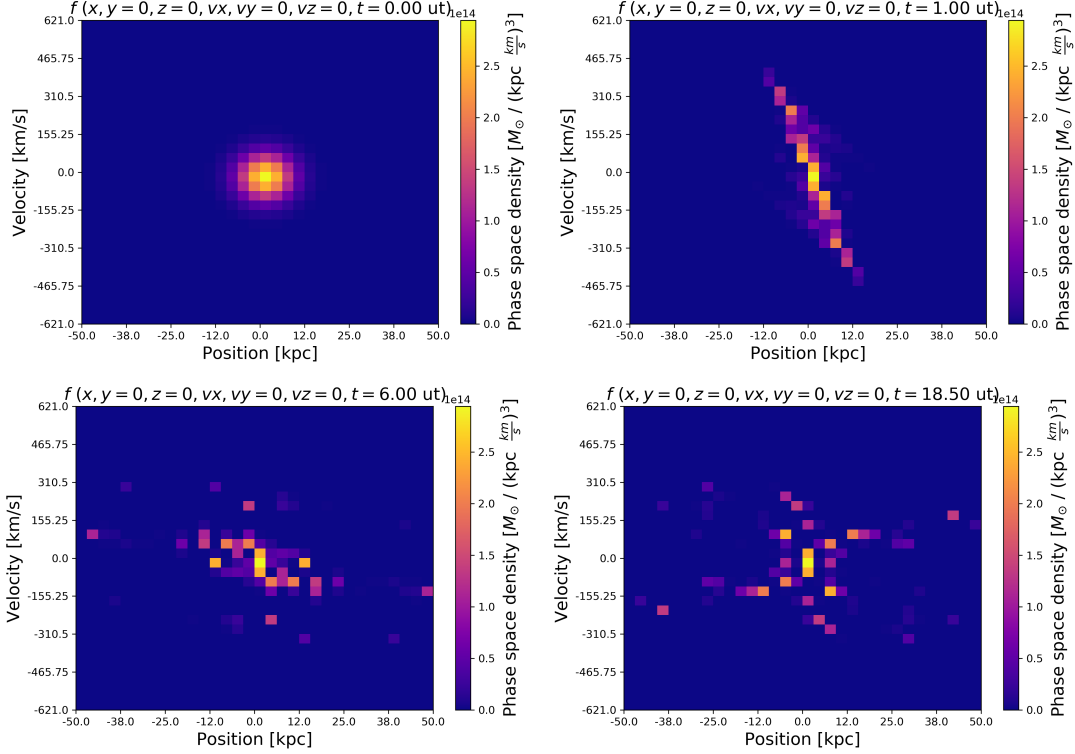


Figure 3.10: A two dimensional cut of the six dimensional phase space. Due to the low resolution, the phase space cannot form its typical spiral but evolves into a gas without any apparent structure. In the upper frames the phase space is still trying to form the spiral. In the bottom two frames the lattice noise has already destroyed the arm structure.

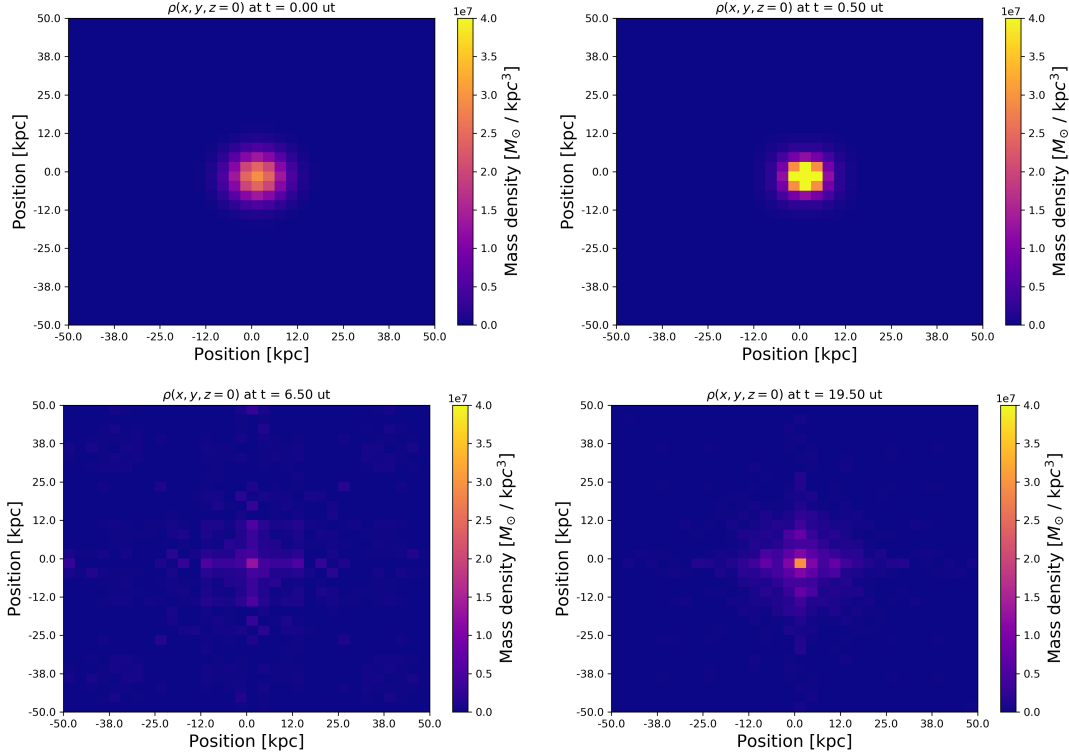


Figure 3.11: A two dimensional cut of the three dimensional volumetric density. Upper left: initialization of the density. Upper right: initial collapse of the density. This is the highest peak achieved in the run. Bottom left: the density in the first local minima after the initial collapse. Bottom right: the second maxima of the density distribution. Note the cross in the last two frames, these are a result of the lattice noise.

# Chapter 4

## Results

In this chapter we discuss the results of the collisional runs of the simulation and the study of Bullet Cluster-like distribution.

### 4.1 The two dimensional phase space

#### 4.1.1 Collisional Gaussian distribution

We ran the collisional Gaussian conditions with exactly the same parameters as in the collisionless case and observed the evolution of the phase space. The value of  $\tau$  implies a very small collisional term. Therefore, if we looked at the phase space distribution of the collisional case in the same way as we did in the last section, we would not be able to spot any difference between the two cases. Instead of plotting the phase space of the collisional case, we choose to plot the percentage difference

between the cases

$$P = 100 \left( \frac{f_\tau(\mathbf{r}, \mathbf{v}, t) - f_0(\mathbf{r}, \mathbf{v}, t)}{f_0(\mathbf{r}, \mathbf{v}, t)} \right). \quad (4.1)$$

With  $P$  being the percentage difference of the collisional case with the collisionless case. This representation will allow us to interpret more easily the effects of the collisional term in the distribution.

The evolution of the percentage difference in the phase space between the two cases can be seen in figure 4.1. In it we can appreciate two main regions: a blue region (dominated by collisionless dark matter), and a red region (dominated by collisional dark matter). The collisionless fluid has higher velocities in the centre of the spatial distribution (the blue region), but the collisional distribution has a higher density in the tails of the Gaussian, implying a lower central density peak. This lower central peak in the spatial density can be observed directly in figure 4.2, where values higher than zero correspond to higher collisional density, and lower than zero to a higher collisionless density. Now it is easy to see that the collisional peak is about 20 percent lower than its collisionless counterpart and remains that way, even after a very long time.

Recapitulating, due to the collisional term we have two main effects:

- There is a considerable reduction of velocity in the central part of the spatial distribution.
- There is a reduction of about 20% in the height of the central peak. Additionally, the regions outside the central peak have a higher velocity than their collisionless counterparts.

#### 4.1. THE TWO DIMENSIONAL PHASE SPACE

---

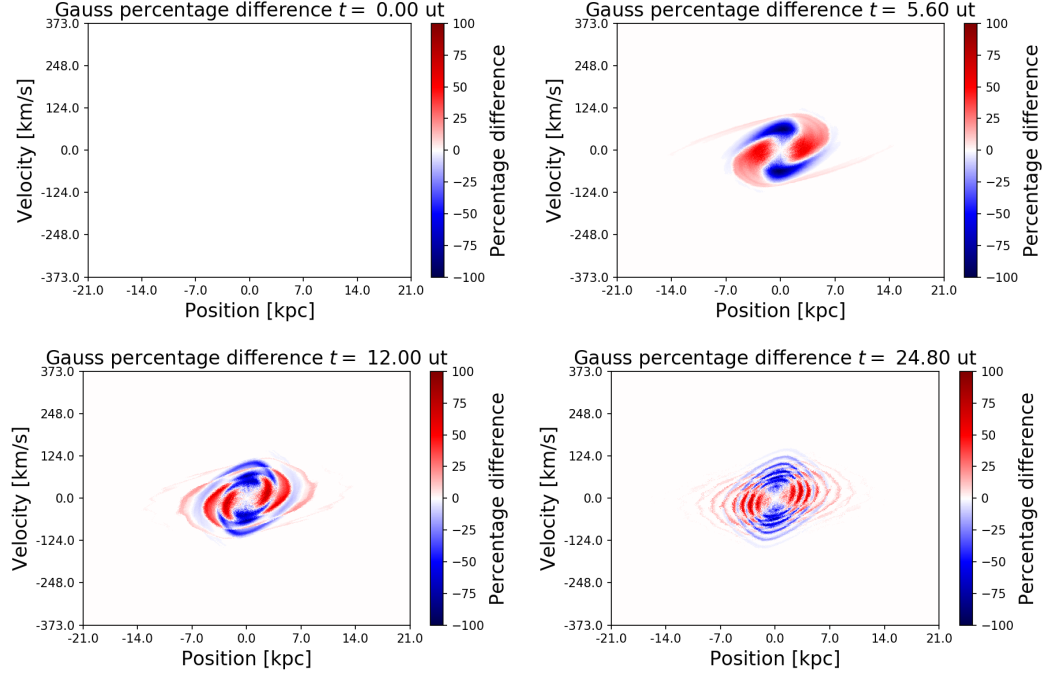


Figure 4.1: Upper left:  $P$  at  $t = 0$ , we had exactly the same initial conditions in both cases. Upper right:  $P$  several timesteps after initialization. The collisional part has already a lower central peak and lower velocities in the centre. Bottom left: Eventually, the *arms* of the distributions get out of sync but the general behavior remains. Bottom right: the distribution from the upper right image is now tainted by the arms. However, the general behavior is still the same, even after a long while.

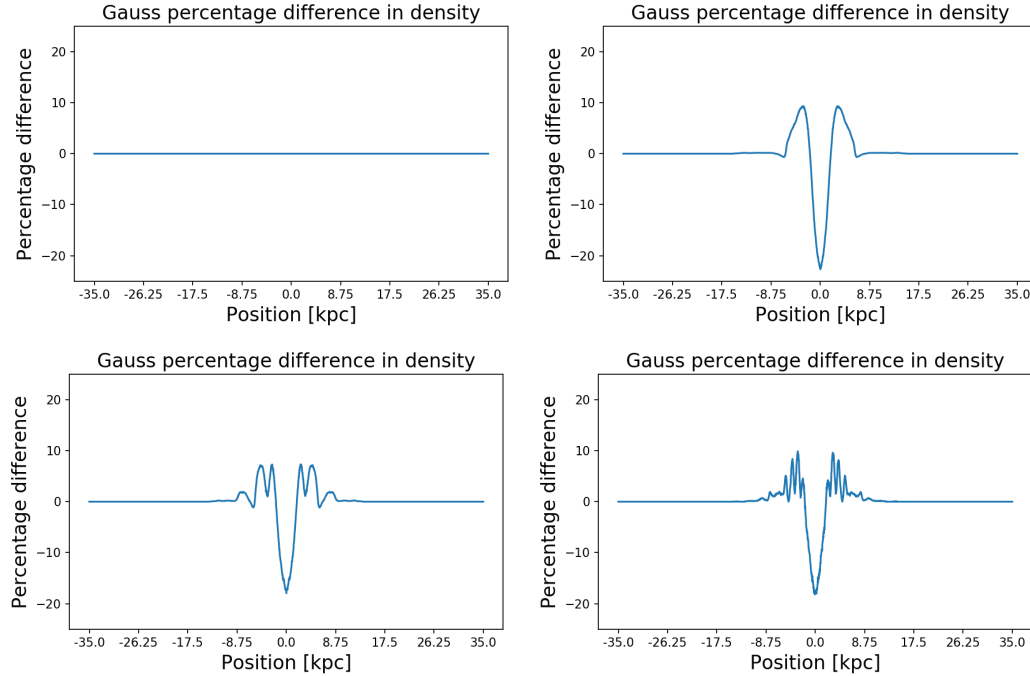


Figure 4.2: Upper left: we initialize both cases with the same distribution. Upper right: after a while the collisionless case already dominates the central region and the collisional the tails. Bottom left: we observe small *oscillations* in the tails but the general behavior remains. Bottom right: after a long while, the tails have some oscillations, nonetheless, the general behavior still remains. The oscillations correspond phase between the little bumps mentioned in the collisionless Gaussian case. Every density frame corresponds to the same frame in figure 4.1.

### 4.1.2 The Bullet Cluster

Having discussed the Gaussian collisional behavior we can proceed to the most interesting initial condition: the Bullet Cluster-like scenario. In which two Gaussian

## 4.1. THE TWO DIMENSIONAL PHASE SPACE

---

distributions of mass collide due to their gravitational interaction, each Gaussian having its very own variance and amplitude. In the real Bullet Cluster one of the clusters was heavier than the other, therefore, we also fix one halo heavier in our simulation.

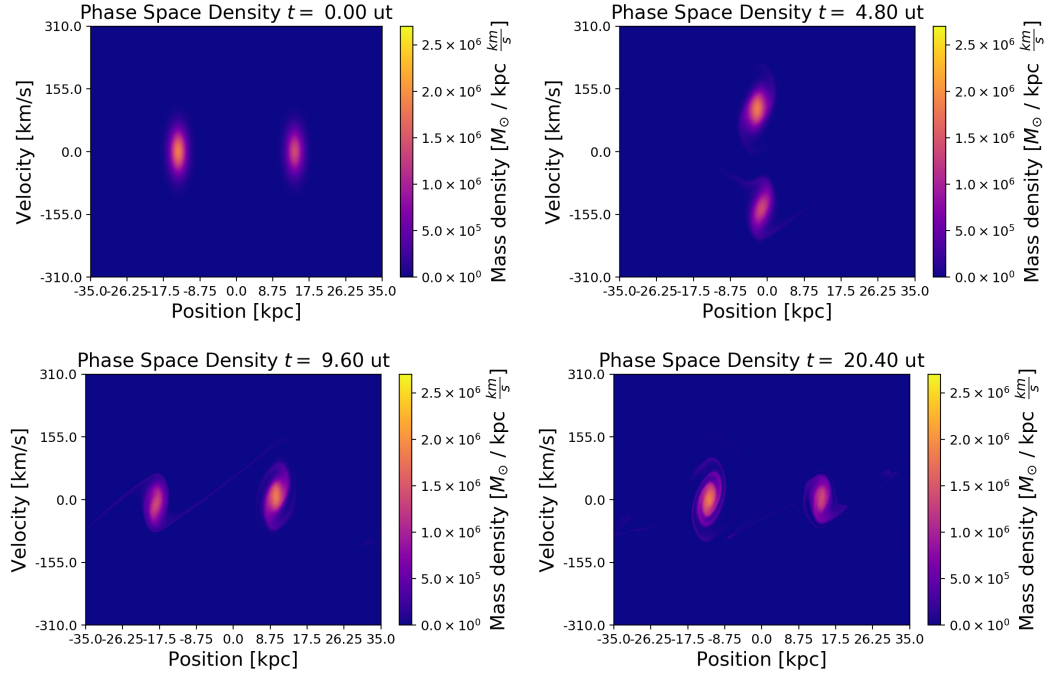


Figure 4.3: Upper left: phase space initialization of the *Bullet Cluster* run. The right halo is slightly less massive (darker). Upper right: phase space during the spatial collision of the halos. The gap in the velocity axis keeps the halos decoupled. Bottom left: phase space with the position of the halos switched regarding the centre of mass and the initial conditions. Bottom right: the system after a full period. The halos are at their initial position but their velocities have changed due to the evolution of each Gaussian.

First we run the collisionless simulation. We expect the halos to simply pass through each other and then gravitate back to collide again. In other words, the *density* profiles will have a periodic movement and will eventually return to their initial

location. In the phase space we see that each halo forms the clockwise spiral from the Gaussian initial conditions. In addition to that, we can see how when the halos occupy the same spatial position they have very different velocities, which keeps them decoupled. The evolution of the phase space can be seen in figure 4.3 and the oscillations of the spatial density can be seen in figure 4.4.

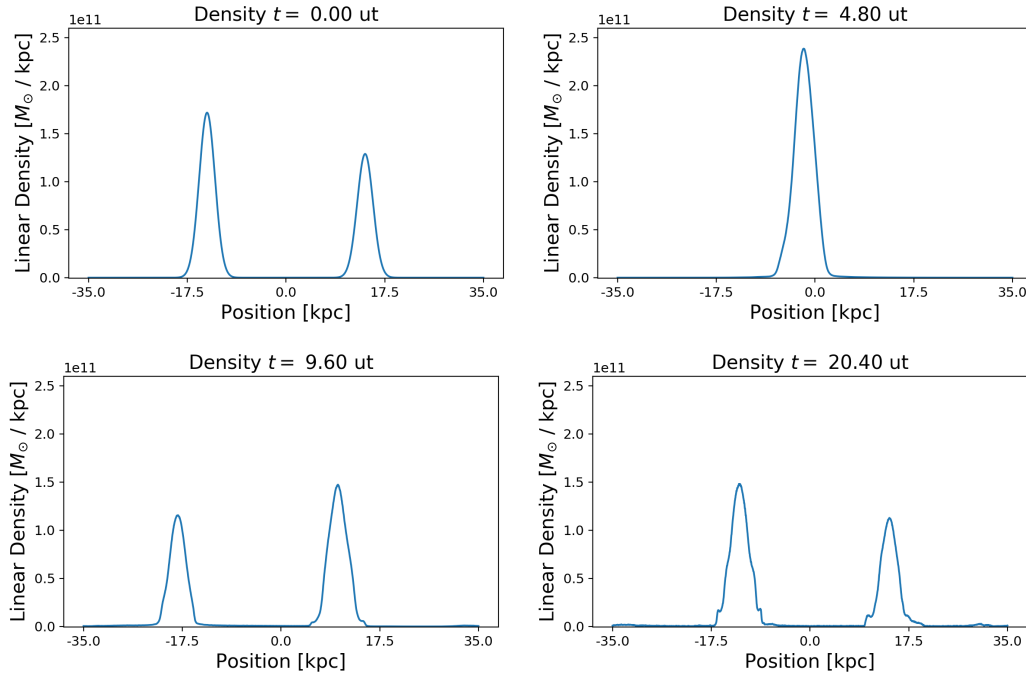


Figure 4.4: Upper left: density initialization of the *Bullet Cluster* run. Notice that the left halo is heavier. Upper right: density during the spatial collision of the halos. Bottom left: density when the halos have switched position with regards to the centre of mass. Bottom right: the system after a full period. The halos are at their initial position but their velocities have changed.

Recalling from 1.1.3, Galaxy Clusters have three main components: a highly collisional baryonic gas, a collisionless distribution of galaxies, and a slightly collisional dark matter halo. Here, we simulated the slightly collisional dark matter component and compare it with the collisionless case.

## 4.1. THE TWO DIMENSIONAL PHASE SPACE

---

For this run we use the same simulation parameters as those of the collisionless case. In the collisionless run the halos had a periodic movement, that was because there was no dissipation of energy. Now that we include short range interactions, there is a loss of energy every time the halos collide (in addition to the loss of energy due to the internal evolution of each collisional Gaussian halo), and because of that, the halos will not return to their initial state. How long will it take for the halos to permanently merge is directly related to the relaxation time. Our relaxation time (8972 ut) is quite high, which is why we expect them to merge only after several collisions.

In figure 4.5 we plot the phase space during the aphelion of the halos, expecting the distance between them to become smaller as time passes by. It is easy to appreciate that the system is permanently loosing energy and is bound to collapse. After six collisions, the smaller halo becomes a current in the bigger one forming a single final halo. This is a very different behavior from the collisionless case, in which the halos could oscillate forever. In figure 4.6 we plot the spatial density at the same time instants as in figure 4.5. It is clear that the halos are getting closer and will eventually merge. Notice that in the final frame, even though the halos have merged, the smaller halo is mostly around the heavier one and will fall inwards given enough time.

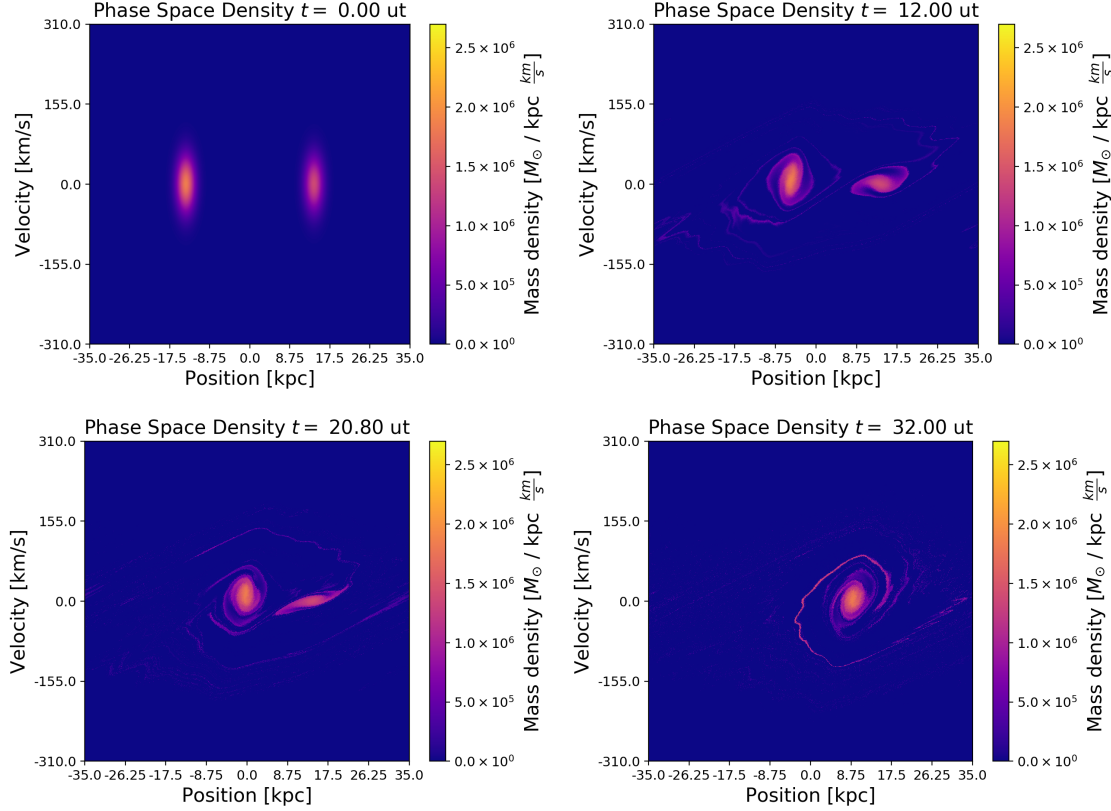


Figure 4.5: Upper left: initial conditions for the phase space of the collisional Bullet Cluster scenario. Upper right: the phase space during the second aphelion since initialization. Note that the halos are closer together now as they have collided twice. Bottom left: the phase space at the fourth aphelion since initialization, the halos have collided four times. The smaller halo is already collapsing towards the bigger one. Bottom right: the smaller halo has already collapsed into a current of the bigger halo.

Finally, we close the two dimensional results comparing the phase space evolution of the collisional case with its collisionless counterpart. We plot the percentage difference  $Z$  as defined for the Gaussian case in figure 4.7. The first frame shows the distributions at their first aphelion, here the two distributions are not too different but the halos of the collisional case are closer together. In the second frame we

#### 4.1. THE TWO DIMENSIONAL PHASE SPACE

---

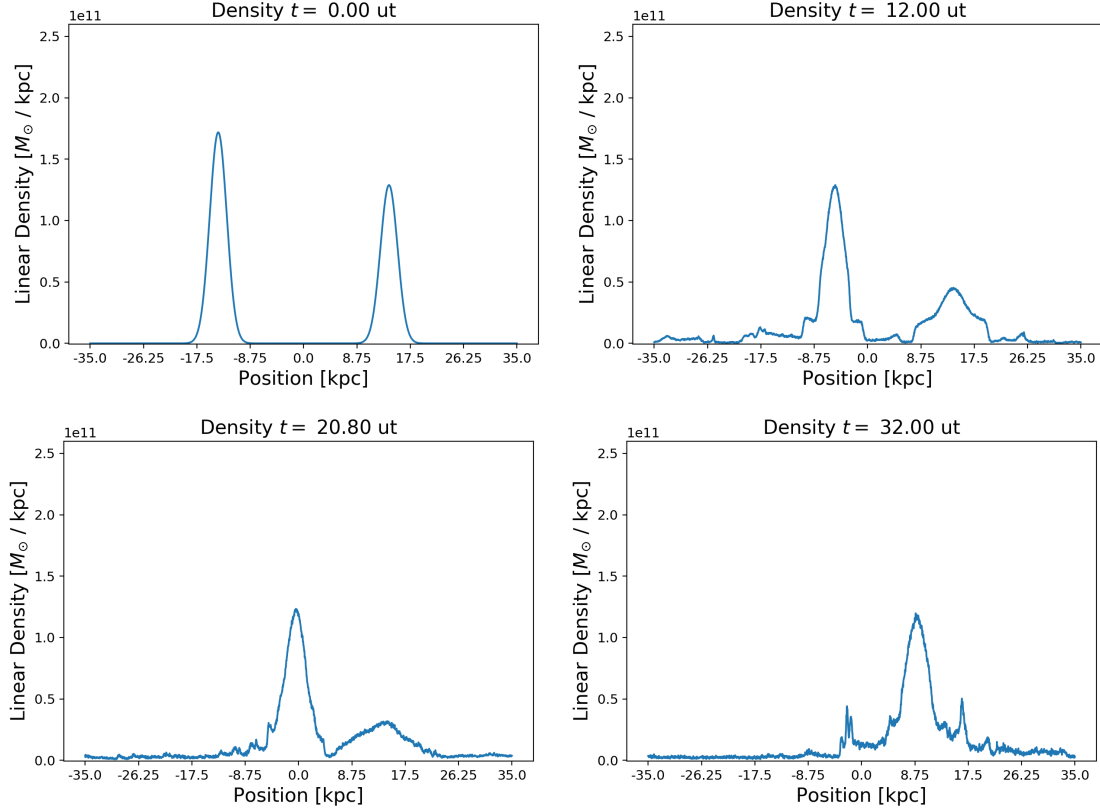


Figure 4.6: The spatial densities correspondent to the frames of figure 4.5. Upper left: initial conditions. Upper right: density during the second aphelion. We observe that there are more bumps than in the collisionless case and the Gaussians are closer. Bottom left: spatial density during the fourth aphelion. The distributions are now even closer, and the smaller Gaussian is starting to be absorbed by the bigger Gaussian. Bottom right: the spatial density at what would have been the sixth aphelion. The halos have merged now, but there are still some oscillations on the tails of the remainder distribution.

observe the collisional distribution on its second aphelion, but the collisionless distribution (blue) has barely moved. The third frame is during the second aphelion of the collisionless distribution, and shows that the collisional halos are already collapsing into one heavier halo. The last frame shows the fourth aphelion of the collisionless

case, here, the smaller halo of the collisional distribution has collapsed into a current in the bigger halo.

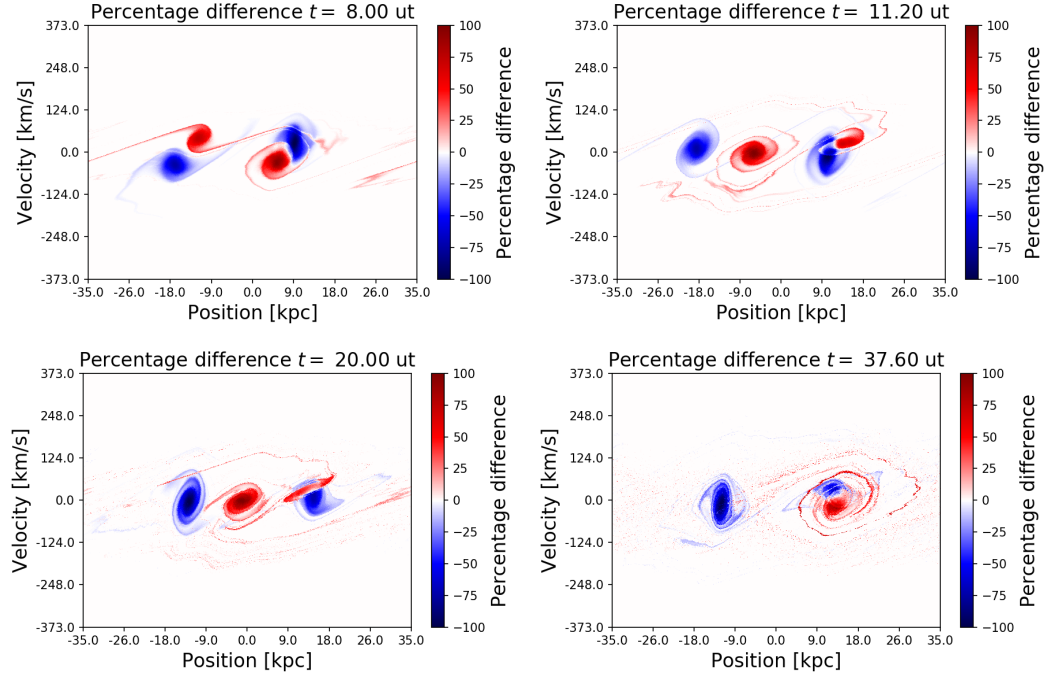


Figure 4.7: Upper left: percentage difference at half the period of the collisionless case. Here they have collided once. Upper right: the collisional distribution has completed one oscillation, meanwhile, the collisionless fluid has barely moved since last frame. Bottom left: the collisionless distribution has completed a period. The collisional smallest halo is already collapsing into a current of the heavier halo. Bottom right: the collisionless distribution has once again completed a period (has collided four times in total). The smallest collisional distribution has been completely torn apart by the heaviest and is now just a current in the outskirts of the final distribution

## 4.2 The four dimensional phase space

We tested the collisionless case of the four dimensional phase space during the numerical tests of section 3.2. Now, for the collisional case we are going to use the Gaussian conditions. As in the collisional case from last section, we do not plot the time evolution of the cut  $f(x, 0, vx, 0)$  of the phase space, but the percentage difference  $P$  between the cuts as defined in equation 4.1.

In figure 4.8 we plot the time evolution of  $P$ . The general form of  $P$  is exactly the same as in figure 4.1, where the collisional case (red) agglomerates outside of the central peak with low velocity, and the collisionless case agglomerates in the central peak with higher velocity than its collisional counterpart. Once again the collisional term implies a reduction in the central density peak along with lower velocities in general.

From the results of comparing the percentage difference of the cuts of the phase space, we can expect the density distribution of the collisional case to have a lower central density peak and heavier tails than its collisionless counterpart. To see more clearly the behavior of the collisional density, we plot in figure 4.9 the percentage difference, now defined as:

$$P = 100 \left( \frac{\rho_\tau(\mathbf{r}, t) - \rho_0(\mathbf{r}, t)}{\rho_0(\mathbf{r}, t)} \right) \quad (4.2)$$

To conclude this section, the influence of the collisional term in the four dimensional phase space is the reduction of the density of particles in the central peak of the spatial distribution, along with an increase in the velocity and density of the regions

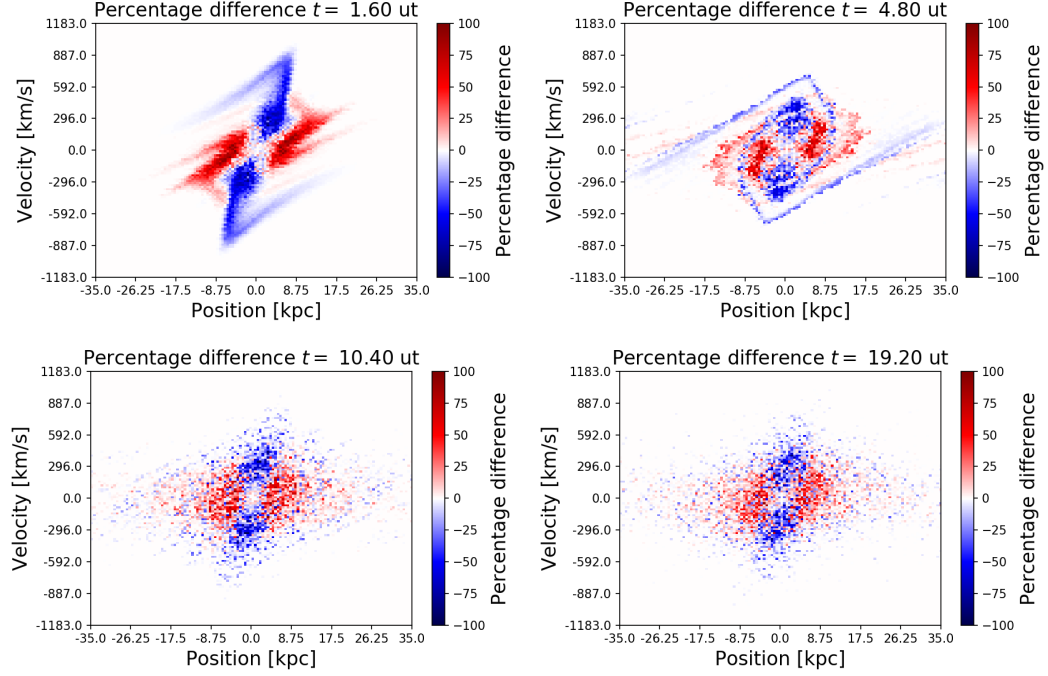


Figure 4.8: Upper left P at  $t = 1.6$  ut. Here the collisionless part has already a higher concentration of mass with higher velocity in the central region. We also observe a higher concentration of the collisional case right outside the central peak. Upper right: as time progresses both distributions start forming their typical clockwise rotating spiral. Besides the arms, the distributions still have the same organization as in last frame. Bottom left: due to the relatively low resolution, the arm structure of the distributions is barely visible anymore, however, the general behavior can still be recognized. Bottom right: the arm distribution cannot longer be resolved and again, the collisional density has a lower central peak. This shows that the behavior is indeed general and is retained even after a very long time.

immediately outside the central peak (the tails of the distribution). These were the same effects we listed in at the end of last section.

## 4.2. THE FOUR DIMENSIONAL PHASE SPACE

---

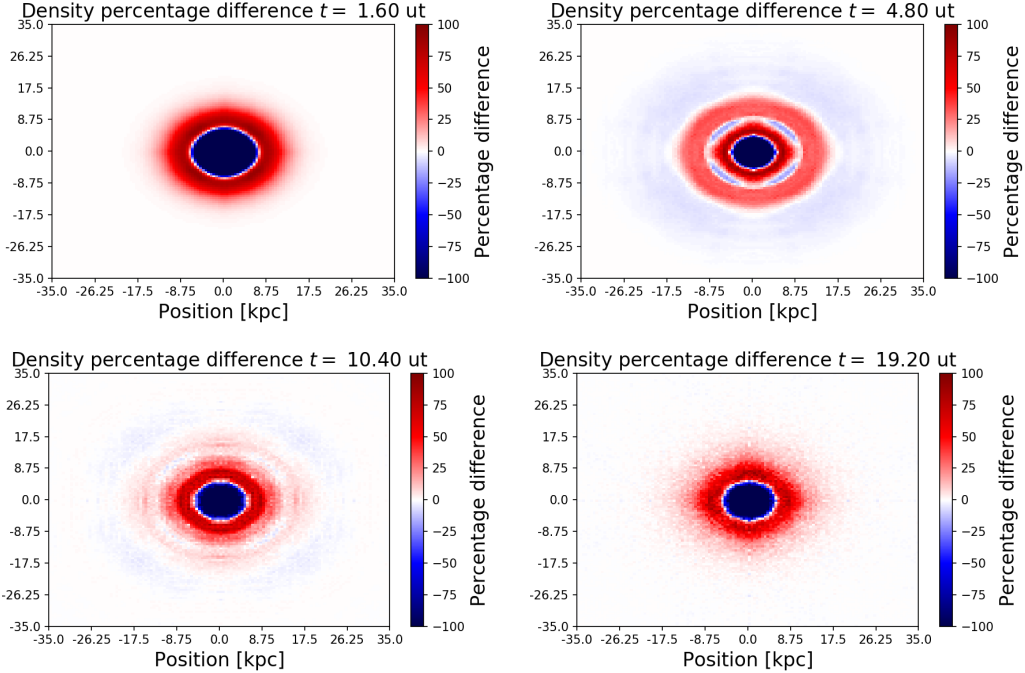


Figure 4.9: Upper left:  $P$  at  $t = 1.6$  ut. Here we observe that the collisionless distribution (blue) already dominates the central peak, and the collisional one has heavier tails. Upper right: the collisionless distribution still dominates the central peak. We also observe that the mass bumps expelled by the collisionless distribution are out of sync with the ones emitted from the collisional one. Also the radius of the central peak has decreased Bottom left: just as in the two dimensional phase space, the mass bumps expelled taint the collisional distribution (red), regardless, the general behavior remains. Bottom right: after a long time the mass bumps become more uniform but the peak of the collisional distribution is still lower, just as in figure 4.2.

# Chapter 5

## Conclusions

We simulated the phase space of a collisional dark matter fluid by implementing a Lattice-Boltzmann method that uses the BGK approximation parameterized by a relaxation time  $\tau$  to model the short range interactions.

We set the relaxation time equivalent to a *thermally averaged cross-section*  $\langle\sigma v\rangle$  of  $3 \times 10^{-26}$  cm<sup>3</sup>/s, a cosmological matter density of  $\Omega_m = 0.312$ , and a mass of the dark matter particle of 0.7 KeV. The origin of these values is discussed in section 2.2. The final value of  $\tau$  depends on the units used in the simulation, for the two dimensional phase space simulation the value of  $\tau$  is 8972. However, we can test dark matter particle candidates by setting different values for  $\langle\sigma v\rangle$  and the mass of the particle.

We successfully implemented a two dimensional phase space simulation in which we tested three initial conditions: Gaussian distribution, Jeans instability, and the collision of two Gaussian distributions. The first two were used to test the code, and

---

to reproduce previous work done on collisionless dark matter fluids. In the first case the distribution evolved into a rotating spiral, the spatial density kept its Gaussian profile. In the Jeans instability scenario we had essentially the same behavior, but this time instead of a single Gaussian profile we had three (because of how we initialized the Jeans oscillations). We observed that our implementation is consistent with previous work and with the expected behavior of the distributions. The third case, the Bullet Cluster-like scenario, showed that there was a periodic movement for the position of the clusters, and the same rotating spiral for the evolution in the phase space of each Gaussian distribution. This was the expected behavior in the absence of a collisional term.

We studied the effects of the collisional term using the Gaussian initial conditions, and Bullet Cluster-like initial conditions. From the first case we concluded that the collisional term reduces the height of the central peak of the spatial density distribution by about 20%, also reduces the velocities on the peak, and increases the density in the tails of the spatial distribution. From the Bullet Cluster initial conditions we observed that after a collision the new greatest distance of the halos is smaller. After several collision we observed the halos merging, a behavior impossible in a properly implemented no collisional simulation.

We extended the two dimensional simulation to a four dimensional phase space. To test it, we used Gaussian conditions and obtained a complete analog of the two dimensional phase space. We also compared the collisional case with the collisionless one, only to find again that the height of the central peak of the distribution is lower in the collisional case, that there is a higher concentration of mass in the tails of the spatial distribution in the collisional case, and that the velocities in the central peak

are lower than in the collisionless scenario.

In the four dimensional simulation we could also observe some problems due to the low resolution. The arms of the clockwise spiral that the phase space forms are not longer resolvable in the four dimensional simulation after a few hundred million years. This could be an effect of the lattice noise: due to the low concentrations of mass in the arms of the spirals, the lattice noise is enough to blur them into a simple cloud.

Finally, we extended the four dimensional simulation into a six dimensional one. The increase in the number of dimensions once again brought a decrease in the resolution. The six dimensional simulation required memory larger than was available on a single computing node. One possible solution is to parallelize the code to be able to use larger amounts of memory.

# Chapter 6

## Bibliography

- [1] Philip Mocz and Sauro Succi. Integer lattice dynamics for Vlasov–Poisson. *Mon. Not. Roy. Astron. Soc.*, 465(3):3154–3162, 2017.
- [2] Sebastián Franco Ulloa. Simulaciones de un fluido débilmente auto-interactuante con métodos de lattice-boltzmann. Master’s thesis, Universidad de los Andes, 5 2017.
- [3] Gianfranco Bertone and Dan Hooper. A History of Dark Matter. *Submitted to: Rev. Mod. Phys.*, 2016.
- [4] J. M. Cline. TASI Lectures on Early Universe Cosmology: Inflation, Baryogenesis and Dark Matter. *ArXiv e-prints*, July 2018.
- [5] H. Andernach and F. Zwicky. English and Spanish Translation of Zwicky’s (1933) The Redshift of Extragalactic Nebulae. *ArXiv e-prints*, November 2017.

- [6] M. Schwarzschild. Mass distribution and mass-luminosity ratio in galaxies. 59:273, September 1954.
- [7] Meekins J. F., Fritz G., Chubb T. A., and Friedman H. Physical Sciences: X-rays from the Coma Cluster of Galaxies. 231:107–108, May 1971.
- [8] A. Penzias. Free Hydrogen in the Pegasus I Cluster of Galaxies. 66:293, March 1961.
- [9] I S. Chandrasekhar. The time of relaxation of stellar systems. 93:285, 02 1941.
- [10] D. H. Rogstad and G. S. Shostak. Gross Properties of Five Scd Galaxies as Determined from 21-CENTIMETER Observations. 176:315, September 1972.
- [11] M. S. Roberts and R. N. Whitehurst. The rotation curve and geometry of M31 at large galactocentric distances. 201:327–346, October 1975.
- [12] V. C. Rubin and W. K. Ford, Jr. Rotation of the Andromeda Nebula from a Spectroscopic Survey of Emission Regions. 159:379, February 1970.
- [13] J. P. Ostriker, P. J. E. Peebles, and A. Yahil. The size and mass of galaxies, and the mass of the universe. 193:L1–L4, October 1974.
- [14] J. F. Navarro, C. S. Frenk, and S. D. M. White. The Structure of Cold Dark Matter Halos. 462:563, May 1996.
- [15] Mariangela Lisanti. Lectures on Dark Matter Physics. In *Proceedings, Theoretical Advanced Study Institute in Elementary Particle Physics: New Frontiers in Fields and Strings (TASI 2015): Boulder, CO, USA, June 1-26, 2015*, pages 399–446, 2017.

## BIBLIOGRAPHY

---

- [16] John S. Gallagher III Linda S. Sparke. *Galaxies in the Universe: An Introduction*. Cambridge University Press, 2 edition, 2007.
- [17] S. S. Gershtein and Ya. B. Zeldovich. Rest Mass of Muonic Neutrino and Cosmology. *JETP Lett.*, 4:120–122, 1966. [,58(1966)].
- [18] P. L. Bhatnagar, E. P. Gross, and M. Krook. A Model for Collision Processes in Gases. I. Small Amplitude Processes in Charged and Neutral One-Component Systems. *Physical Review*, 94:511–525, May 1954.
- [19] Prieto Asinari. *Multi-Scale Analysis of Heat and Mass Transfer in Mini/Micro-Structures*. PhD thesis, Politecnico di Torino, 2005.
- [20] F. Filbet, J. Hu, and S. Jin. A Numerical Scheme for the Quantum Boltzmann Equation Efficient in the Fluid Regime. *ArXiv e-prints*, September 2010.
- [21] V. Fuka. PoisFFT - A Free Parallel Fast Poisson Solver. *ArXiv e-prints*, September 2014.
- [22] J.W Eastwood R.W Hockney. *Computer simulation using particles*.
- [23] Matteo Frigo and Steven G. Johnson. The design and implementation of FFTW3. *Proceedings of the IEEE*, 93(2):216–231, 2005. Special issue on “Program Generation, Optimization, and Platform Adaptation”.
- [24] Planck Collaboration, N. Aghanim, Y. Akrami, M. Ashdown, J. Aumont, C. Baccigalupi, M. Ballardini, A. J. Banday, R. B. Barreiro, N. Bartolo, S. Basak, R. Battye, K. Benabed, J.-P. Bernard, M. Bersanelli, P. Bielewicz, J. J. Bock, J. R. Bond, J. Borrill, F. R. Bouchet, F. Boulanger, M. Bucher,

---

## BIBLIOGRAPHY

C. Burigana, R. C. Butler, E. Calabrese, J.-F. Cardoso, J. Carron, A. Challinor, H. C. Chiang, J. Chluba, L. P. L. Colombo, C. Combet, D. Contreras, B. P. Crill, F. Cuttaia, P. de Bernardis, G. de Zotti, J. Delabrouille, J.-M. Delouis, E. Di Valentino, J. M. Diego, O. Doré, M. Douspis, A. Ducout, X. Dupac, S. Dusini, G. Efstathiou, F. Elsner, T. A. Enßlin, H. K. Eriksen, Y. Fantaye, M. Farhang, J. Fergusson, R. Fernandez-Cobos, F. Finelli, F. Forastieri, M. Frailis, E. Franceschi, A. Frolov, S. Galeotta, S. Galli, K. Ganga, R. T. Génova-Santos, M. Gerbino, T. Ghosh, J. González-Nuevo, K. M. Górski, S. Gratton, A. Gruppuso, J. E. Gudmundsson, J. Hamann, W. Handley, D. Herranz, E. Hivon, Z. Huang, A. H. Jaffe, W. C. Jones, A. Karakci, E. Keihänen, R. Keskitalo, K. Kiiveri, J. Kim, T. S. Kisner, L. Knox, N. Krachmalnicoff, M. Kunz, H. Kurki-Suonio, G. Lagache, J.-M. Lamarre, A. Lasenby, M. Latanzi, C. R. Lawrence, M. Le Jeune, P. Lemos, J. Lesgourgues, F. Levrier, A. Lewis, M. Liguori, P. B. Lilje, M. Lilley, V. Lindholm, M. López-Caniego, P. M. Lubin, Y.-Z. Ma, J. F. Macías-Pérez, G. Maggio, D. Maino, N. Mandlesi, A. Mangilli, A. Marcos-Caballero, M. Maris, P. G. Martin, M. Martinelli, E. Martínez-González, S. Matarrese, N. Mauri, J. D. McEwen, P. R. Meinhold, A. Melchiorri, A. Mennella, M. Migliaccio, M. Millea, S. Mitra, M.-A. Miville-Deschénes, D. Molinari, L. Montier, G. Morgante, A. Moss, P. Natoli, H. U. Nørgaard-Nielsen, L. Pagano, D. Paoletti, B. Partridge, G. Patanchon, H. V. Peiris, F. Perrotta, V. Pettorino, F. Piacentini, L. Polastri, G. Polenta, J.-L. Puget, J. P. Rachen, M. Reinecke, M. Remazeilles, A. Renzi, G. Rocha, C. Rosset, G. Roudier, J. A. Rubiño-Martín, B. Ruiz-Granados, L. Salvati, M. Sandri, M. Savelainen, D. Scott, E. P. S. Shellard, C. Sirignano, G. Sirri, L. D. Spencer, R. Sunyaev, A.-S. Suur-Uski, J. A. Tauber, D. Tavagnacco, M. Tenti,

## BIBLIOGRAPHY

---

- L. Toffolatti, M. Tomasi, T. Trombetti, L. Valenziano, J. Valiviita, B. Van Tent, L. Vibert, P. Vielva, F. Villa, N. Vittorio, B. D. Wandelt, I. K. Wehus, M. White, S. D. M. White, A. Zacchei, and A. Zonca. Planck 2018 results. VI. Cosmological parameters. *ArXiv e-prints*, July 2018.
- [25] S. W. Randall, M. Markevitch, D. Clowe, A. H. Gonzalez, and M. Bradač. Constraints on the Self-Interaction Cross Section of Dark Matter from Numerical Simulations of the Merging Galaxy Cluster 1E 0657-56. 679:1173–1180, June 2008.
- [26] A. Robertson, R. Massey, and V. Eke. What does the Bullet Cluster tell us about self-interacting dark matter? 465:569–587, February 2017.
- [27] K. Bekki and S. Stanimirović. The total mass and dark halo properties of the Small Magellanic Cloud. 395:342–350, May 2009.
- [28] E. Corbelli. Dark matter and visible baryons in M33. 342:199–207, June 2003.